Supplementary Information for

The origin of anode-electrolyte interfacial passivation in rechargeable Mg-metal batteries

Jinlei Zhang,‡[a] Jing Liu,‡[ab] Min Wang,[a] Zhonghua Zhang,*[ac] Zhenfang Zhou,[a] Xi Chen,[d] Aobing Du,[c] Shanmu Dong,[c] Zhenjiang Li,[a] Guicun Li*[a] and Guanglei Cui*[c]

[a] *College of Materials Science and Engineering, Qingdao University of Science and Technology, Qingdao 266042, P. R. China.*

[b] *Department of Pharmacy, Jining Medical University, Rizhao 276826, P. R. China.*

[c] *Qingdao Industrial Energy Storage Research Institute, Qingdao Institute of Bioenergy and Bioprocess Technology, Chinese Academy of Sciences, Qingdao 266101, P. R. China.*

[d] *Department of Physics, Xi'an Jiaotong-Liverpool University, Suzhou 215123, P. R. China.*

‡ J. Zhang and J. Liu contributed equally to this work.

* Corresponding author. E-mail: zhangzh@qust.edu.cn; guicunli@qust.edu.cn; cuigl@qibebt.ac.cn

Experimental section:

Characterization

^1H nuclear magnetic resonance (^1H NMR) characterizations were performed with NMR spectrometer (AVANCE-III 600 MHz). DMSO (Sigma) was sealed in a glass capillary which was inserted into NMR toube to lock the magnetic field during characterizations. For the ^1H NMR characterizations of Figure 1c, pure H_2O, 0.5 mL diglyme + 0.19 mL H_2O, and 0.5 mL diglyme + 0.19 mL H_2O + 0.2338 g $Mg(TFSI)_2$ were performed.

Moisture content characterizations were performed with Karl Fischer moisture titrator (WKT-A9) in the Ar-filled glove box (H_2O < 0.1 ppm, O_2 < 0.1 ppm).

Conventional scanning electron microscopy (SEM) characterizations were performed with JSM-6700F, JSM7500F, and NNS450 scanning electron microscopes.

Conventional transmission electron microscopy (TEM) characterizations were performed with JEM-2100PLUS and JEOL JEM-F200 transmission electron microscopes.

X-ray diffraction (XRD) characterizations were performed with D/MAX/2500PC X-ray diffraction.

X-ray photoelectron spectroscopy (XPS) characterizations were performed with PHI5000 VersaprobeIII XPS (Mono Al Kα, 1486.6 eV, 15 kV, 4.5 mA, CAE mode).

Raman characterization was performed with HORIBA LabRAM HR Evolution.

All cryogenic electron microscopy (Cryo-EM) tests were performed with a Talos 200X TEM under ultra-low temperature of about 95K and operated at 200 kV. All TEM images were obtained with a Ceta camera. STEM images were obtained with HAADF detector, and EDS tests were operated with SuperX energy dispersive spectroscopy.

Electrolyte preparation

0.4 M $Mg(TFSI)_2$/diglyme electrolyte: 0.468 g $Mg(TFSI)_2$ and 2 mL diglyme (Sigma-Aldrich, 99.5%) were added into a 5 mL vial in the Ar-filled glove box (H_2O < 0.1 ppm, O_2 < 0.1 ppm), which were stirred for at least 1 hour under 400 rpm. $Mg(TFSI)_2$/diglyme electrolytes with other concentrations were prepared in the same way with different amount $Mg(TFSI)_2$.

The $Mg(TFSI)_2$ reagents were purchased from Macklin (97%, $Mg(TFSI)_2$-M), Energy Chemical (98.0%, $Mg(TFSI)_2$-E), DoDoChem (99.0%, $Mg(TFSI)_2$-D), and Solvionic (99.5%, $Mg(TFSI)_2$-S). **If no otherwise specified, $Mg(TFSI)_2$ reagent used is $Mg(TFSI)_2$-M**. All phenyl complex (APC, 41.2% 2 M MgPhCl/THF, 5.3% $AlCl_3$, 53.4% THF) electrolyte was purchased from DoDoChem. Di-N-butylmagnesium (1.0 M in THF) was purchased from Macklin. Isobutylamine (IBA, 99.5%) was purchased from Energy Chemical.

Batteries assembly and electrochemical tests

All electrochemical performance characterizations were conducted with 2032-type cells. Mg foil (0.1 mm in thickness, 12 mm in diameter), Cu foil (12 mm in diameter), GF separator (GF/D, Whatman, 16 mm in diameter), and PI separator (16 mm in diameter) were used for cell assembling in Ar-filled glove box. 180 µL electrolytes were dropped on GF separator. After assembling, the cells were compacted by Compact Crimping Machine (MSK-160E, HEFEI KEJING MATERIALS TECHNOLGY CO, LTD.) with the pressure of 1T. All galvanostatic charge-discharge (GCD) tests were performed with LAND batteries testing system (CT2001A and CT3002A).

The transference number of Mg ions ($\tau_{Mg-ions}$) is equal to I_s/I_0, where I_0 is the initial current and I_s is

the current after stable. Thus, the $\tau_{Mg\text{-ions}}$ calculated in this case is about 0.35 (8.63E–8/2.47E–7). Applied voltage is 100 mV.

Molecular dynamic simulation

Ions involved in simulation were processed with 0.8 scale OPLS-AA force field[1]. Other molecules were optimized by Gaussian16 with a level of B3LYP/def2tzvp to obtain reasonable structures. The force field parameters were obtained from Ligpargen[2-4]. The initial structures of simulation system were produced by Packing Optimization for Molecular Dynamics (MD) Simulations (Packmol) program[5]. And the size of periodic box was 5*5*5 nm³. Molecule dynamics simulations were carried out with gromacs 2019.5 package. Detailed simulation processes are shown below[6,7]. (1) To avoid inconsequent contacts, 5000 steeps steepest descent method and 5000 steeps conjugate gradient method were utilized to optimize system. (2) NPT was utilized to achieve pre-equilibrium of system. V-rescale temperature coupling and Parrinello-Rahman pressure coupling were utilized to control the temperature at 298 K and the pressure at 1 atm. The definition of non-bonding radius was 1.2 nm and the integration step-size was 1 fs. (3) Switching to Berendsen method after system was equilibrium. Bond length and angle were restricted with LINCS algorithm. Van der Waals interactions were utilized, and long range electrostatic interactions were set by particle-mesh Ewald method.

Binding energy

All molecules involved in this section were searched via Molclus software and 10 geometries were produced[8]. The pre-optimization of them were performed via xtb software and the six geometries were obtained in this step[9]. These geometries were further optimized via Gaussian 16 software with a level of B3LYP/def2svp em=gd3bj and the frequency were also calculated at the same level to prevent the imaginary frequency. The single point energy was calculated at a level of B3LYP/def2tzvp em=gd3bj and the binding energy was calculated via the following formula:

E(binding)=E(AB)-E(A)-E(B)

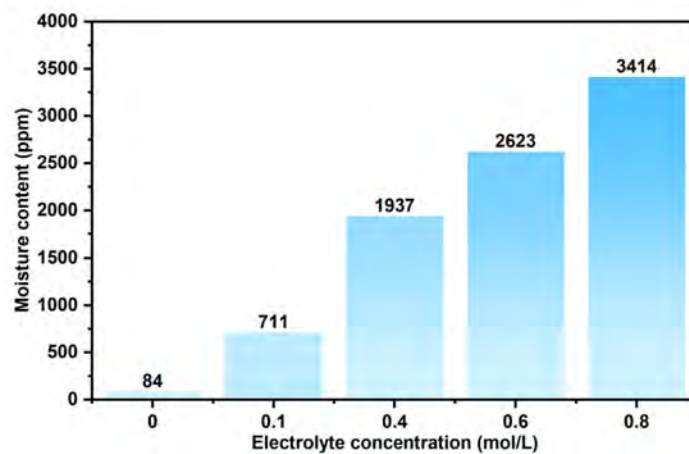**Figure S1**. Moisture content of Mg(TFSI)$_2$(Macklin, 97%)/diglyme electrolytes with different concentrations performed with Karl Fischer moisture titrator.

Moisture content gradually increases with introducing Mg(TFSI)$_2$ reagent.

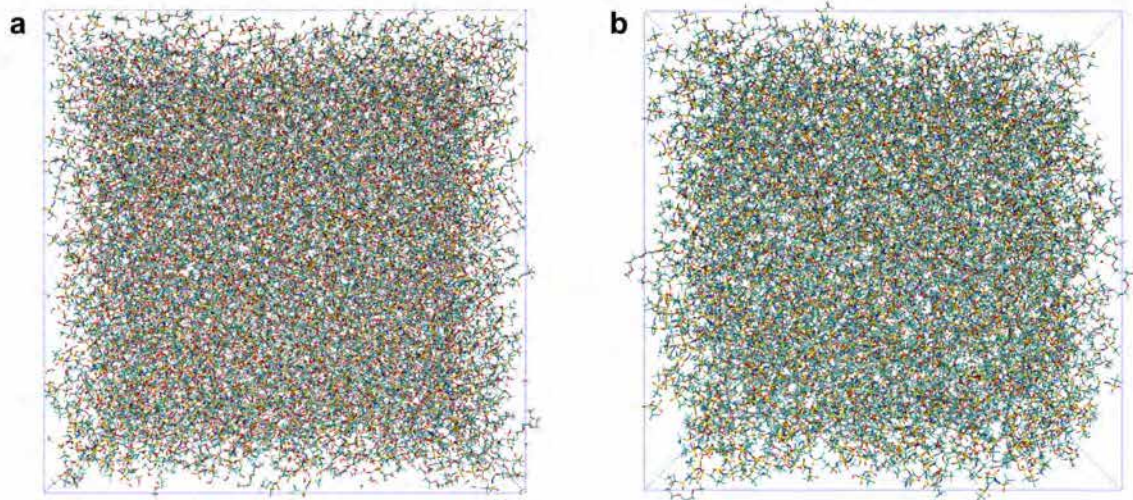**Figure S2**. Snapshots of MD simulation of 0.4 M Mg(TFSI)$_2$/diglyme electrolyte with 0.075 M (1350 ppm) H$_2$O (**a**) and 0.075 mM (1.35 ppm) H$_2$O (**b**).
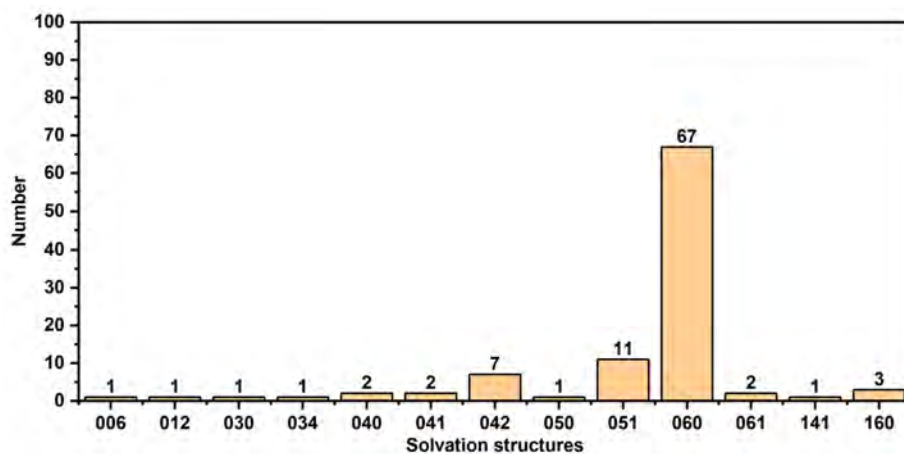
Figure S3. Statistical result of 100 complex structures from MD simulation of 0.4 M Mg(TFSI)$_2$/diglyme electrolyte with 0.075 M (1350 ppm) H$_2$O. Three consecutive numbers in abscissa indicate the complex structures of Mg-ion or Mg^{2+}-anion ion-pairs. (e.g. **141** presents the Mg-ion solvation structure consists of **one** diglyme molecule, **four** H$_2$O molecule, and **one** TFSI anions).
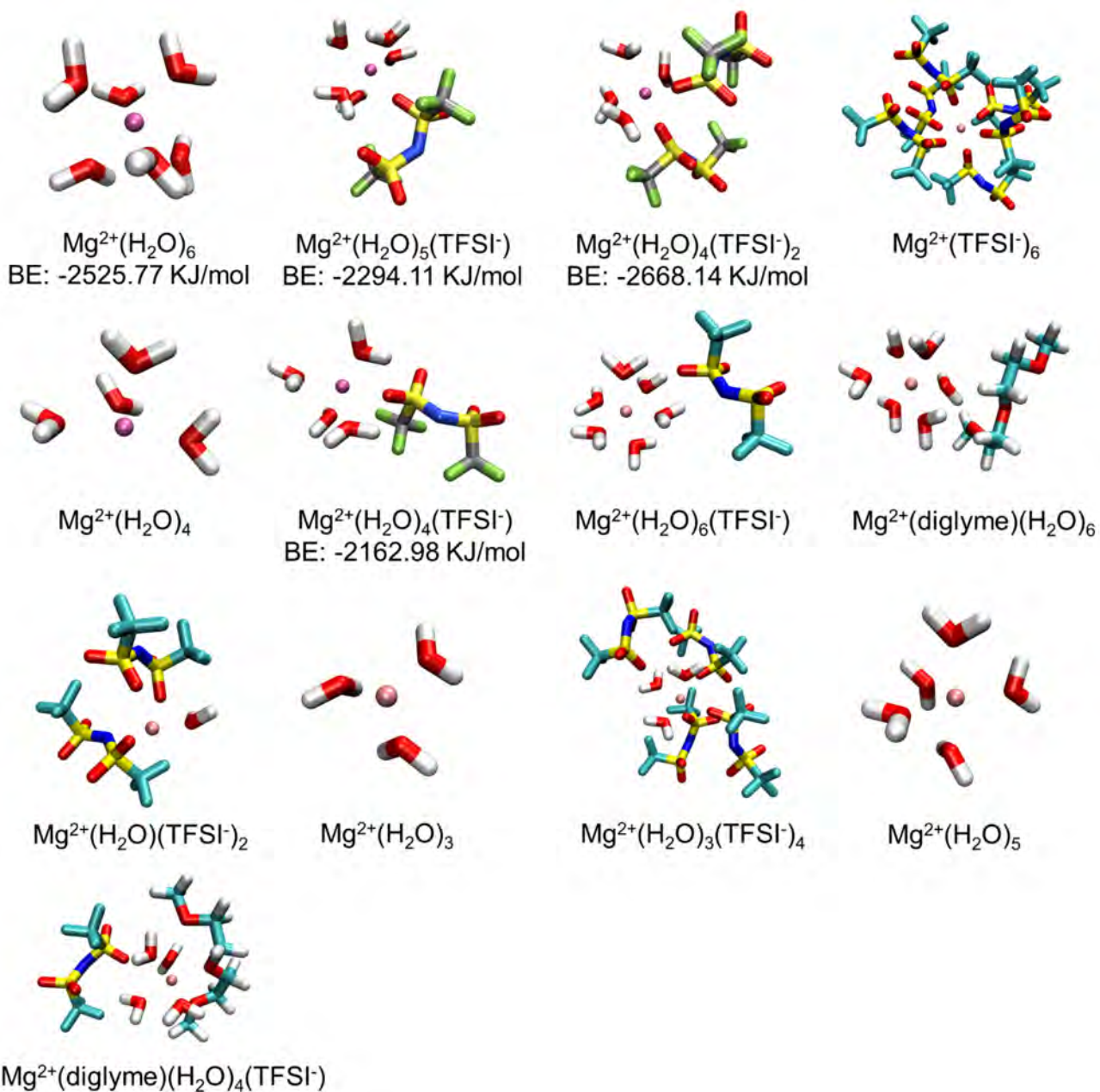
Figure S4. The optimized solvation structures obtained from MD simulation of 0.4 M Mg(TFSI)$_2$/diglyme electrolyte with 0.075 M (1350 ppm) H$_2$O. The partial relative binding energy are also shown.
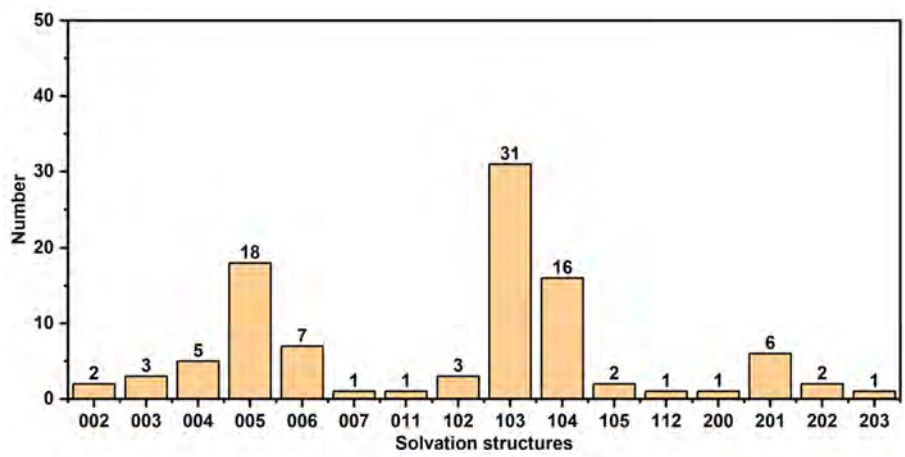
Figure S5. Statistical result of 100 complex structures of MD simulation of 0.4 M Mg(TFSI)$_2$/diglyme electrolyte with 0.075 mM (1.35 ppm) H$_2$O.
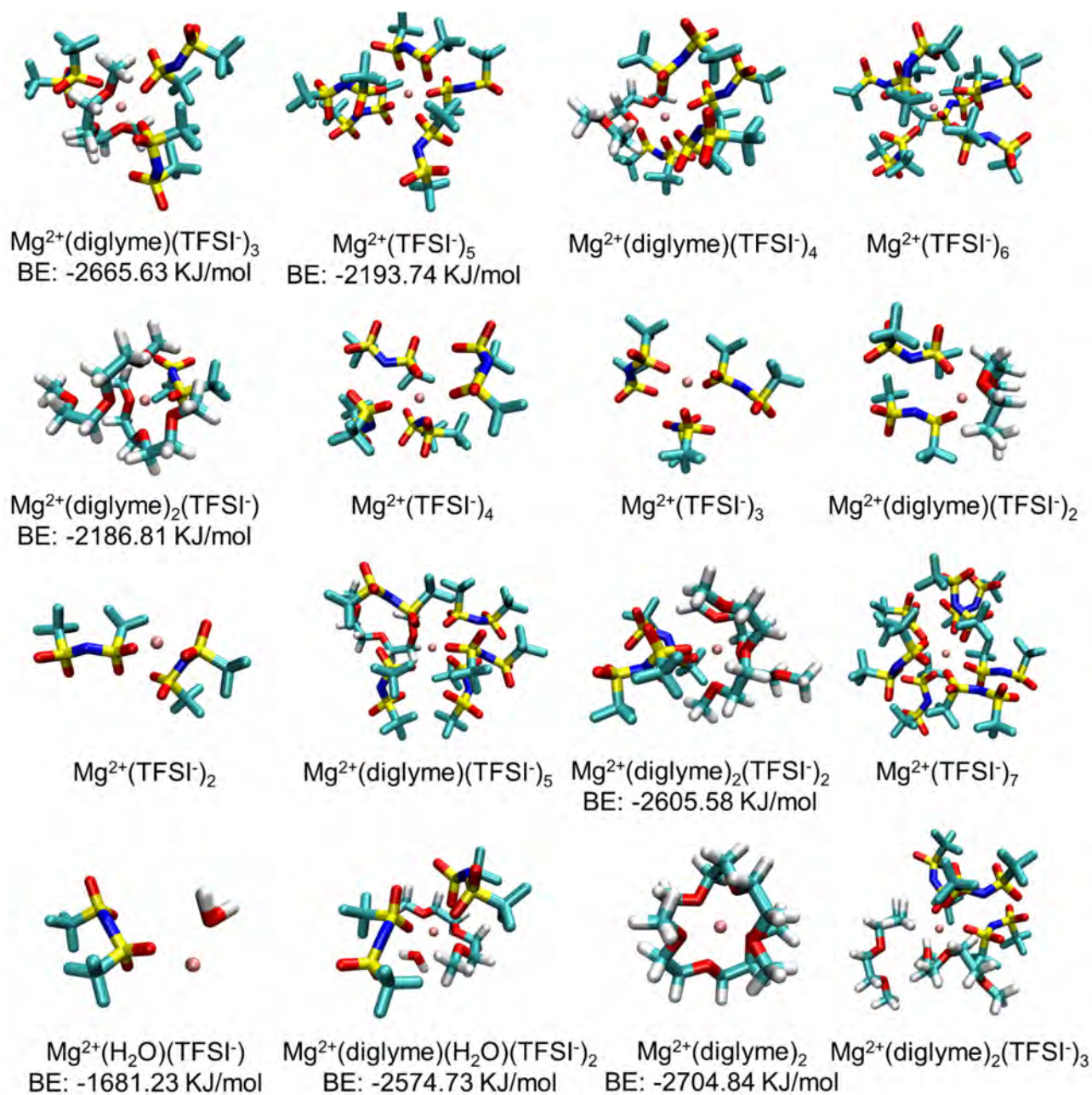
Figure S6. The optimized solvation structures obtained from MD simulation of 0.4 M Mg(TFSI)$_2$/diglyme electrolyte with 0.075 mM (1.35 ppm) H$_2$O. The partial relative binding energy are also shown.
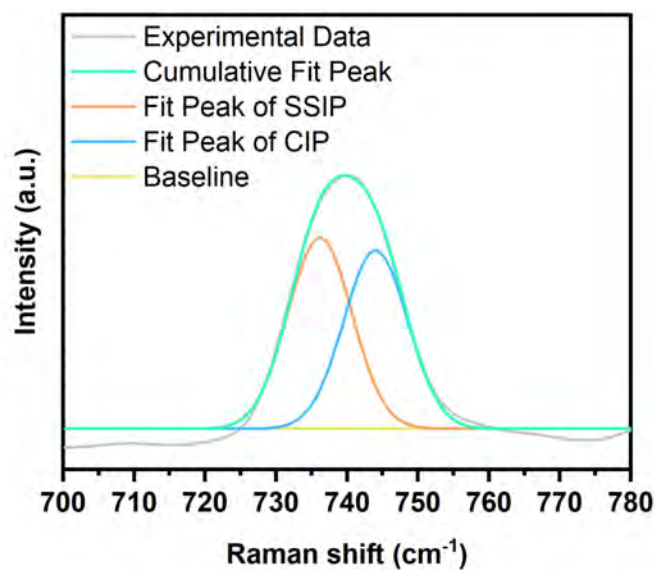
Figure S7. Raman spectrum of 0.4 M Mg(TFSI)$_2$/diglyme electrolyte with the region from 700 to 780 cm^{-1}.

The Raman shift of fitted peaks of solvent separated ion pair (SSIP) and contact ion pair (CIP) are 736.18 and 744.03 cm^{-1}, respectively[10]. This result shows the CIPs occupy a portion of S–N stretching vibration within TFSI anion. The formation of SSIPs might be related to competitive coordination between H$_2$O molecules and TFSI anions in Mg-ion solvation structures. The peak area ratio of SSIP/CIP is equal to about 1.07.
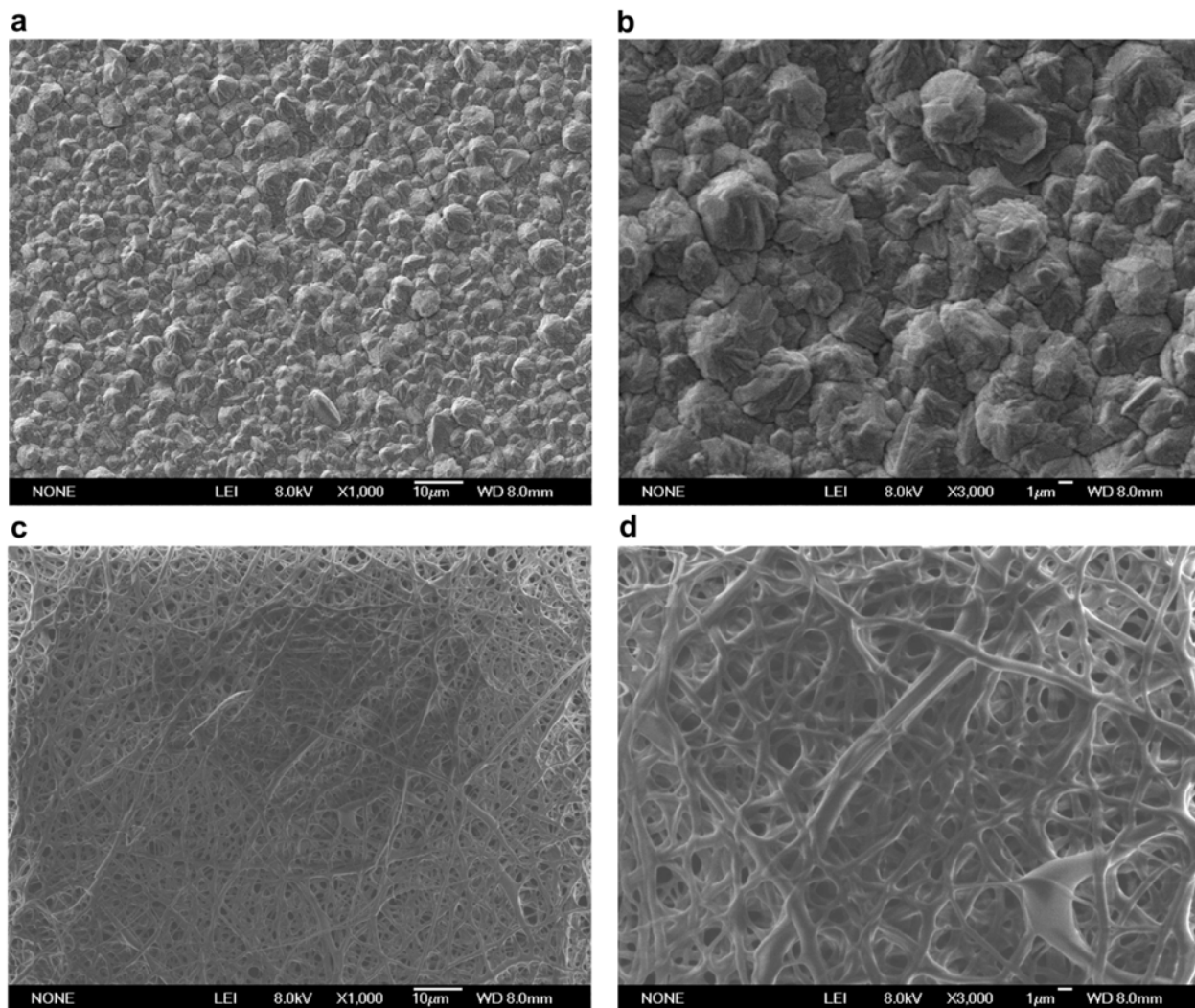
Figure S8. Microstructures of Cu foil and PI separator used for assembling batteries. **a-b**, SEM images of Cu foil with 1000 (**a**) and 3000 (**b**) magnifications. **c-d**, SEM images of PI separator with 1000 (**c**) and 3000 (**d**) magnifications.

Cu particles with several microns are observed. The holes of PI separator also have the size of several microns. The dendritic electrodepositions can easily penetrate these micropores and result in short circuit.
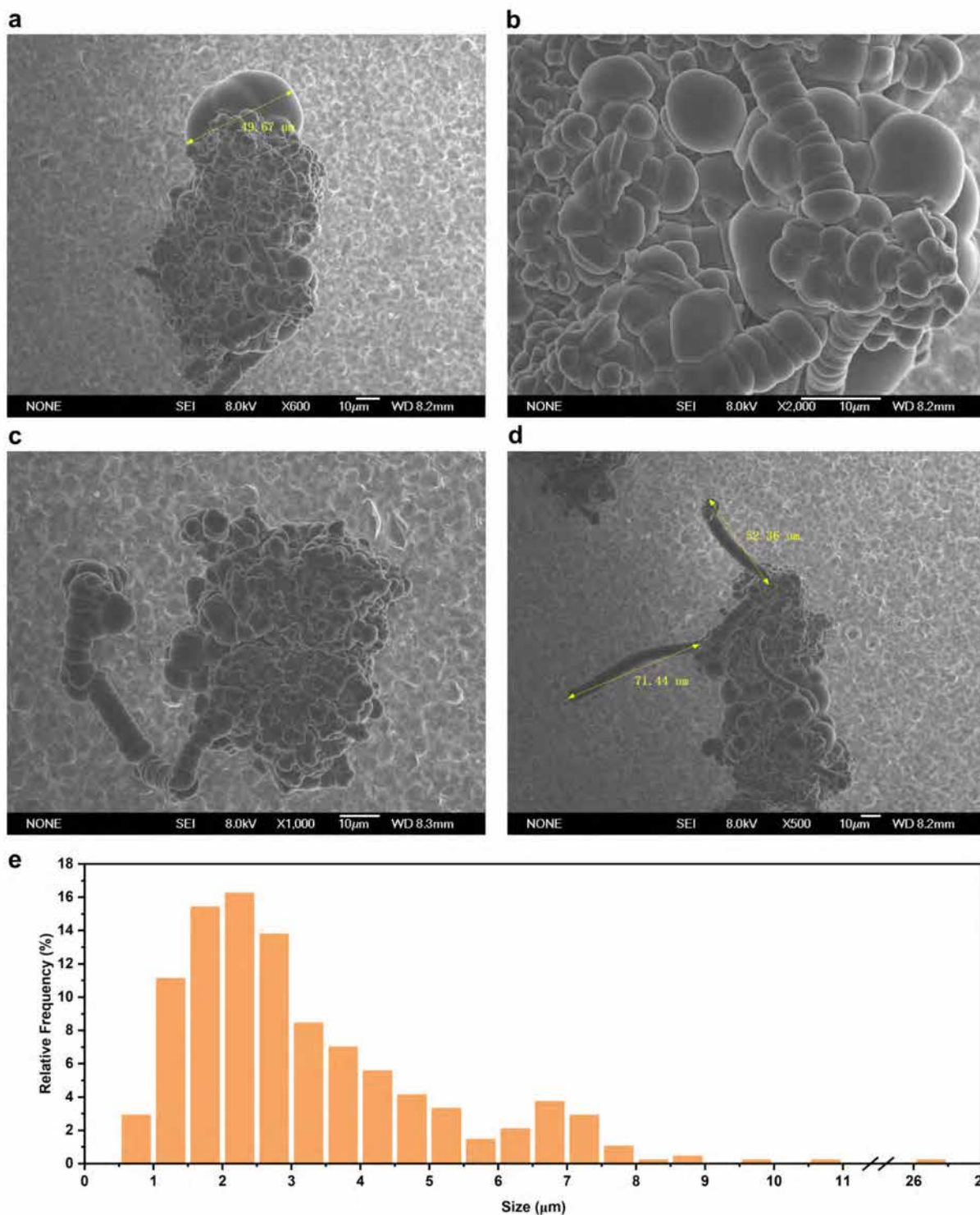
Figure S9. Microscopic morphologies of the electrodepositions on Cu foil electrodes. **a-d**, Typical SEM images of electrodepositions on Cu foil electrode in 0.4 M Mg(TFSI)$_2$/diglyme electrolyte. **e**, Frequency counts of electrodeposition sizes from Figure S9c.

Most of electrodepositions in Figure S9c show the particle size between 1 to 3 μm. The largest size of electrodepositions in Figure S9a is near 50 μm. The length of long wire-like clusters is up to 70 μm as shown in Figure S9d. This 3D growth mode of electrodepositions can easily penetrate into the pores of separators and result in short circuit, which is a threat to battery safety.
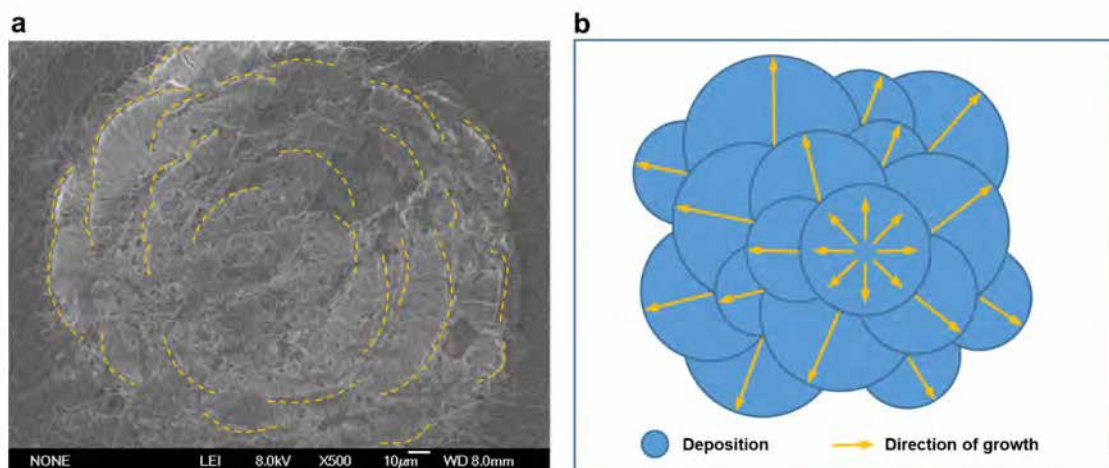
Figure S10. Growth ring trace of the aggregated electrodepositions. SEM image (**a**) and schematic diagram (**b**) of one aggregated electrodeposition adhere to PI separator.

The growth ring trace of the aggregated electrodepositions is clearly observed in this vertical view image, which indicates the continuous nucleation and growth of the electrodepositions. The new nucleation sites are well located on the surface of the electrodeposition microspheres and the newly formed electrodepositions continue to grow into radial or hemispheric shape. This also proves the sphere-on-sphere growth mode observed in Figure S9.
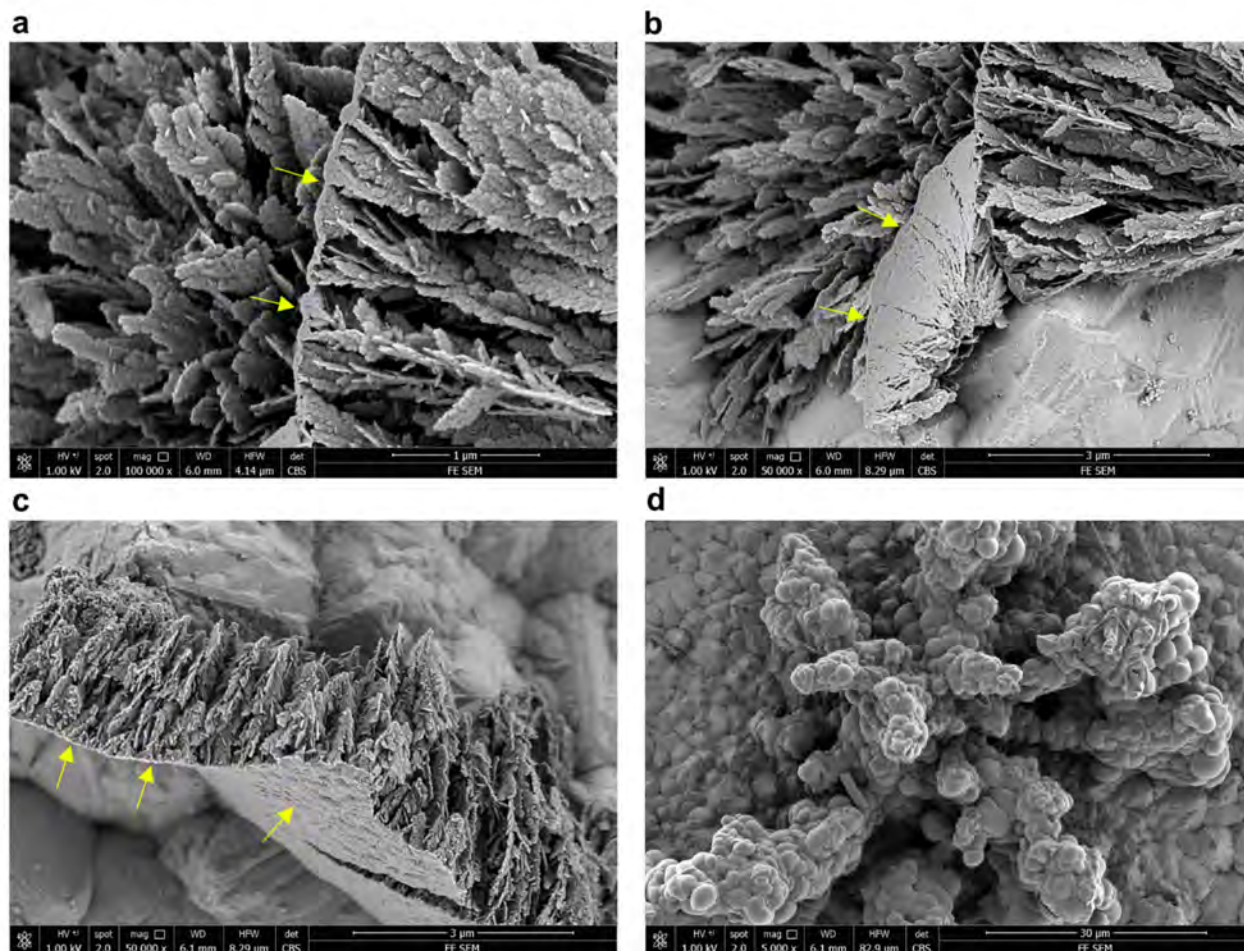
Figure S11. Microscopic morphologies of the electrodepositions from 0.4 M Mg(TFSI)$_2$/diglyme electrolyte. **a-c**, SEM images of the seaweed-like dendritic primary nanostructures consist of extensive stacking slices inside the spherical electrodepositions (**a**, 100000 magnifications; **b** and **c**, 50000 magnifications). The arrows point to the outer shell of the spherical electrodepositions. **d**, The vertically growing spherical electrodeposition with 5000 magnifications.

Figure S11d shows the spherical morphologies of the electrodepositions under 5000 magnifications, which is consistent with previous works[11,12]. Inside the microspheres, however, an intriguing seaweed-like primary nanostructure is observed. These hierarchical electrodeposition microspheres are constructed by the seaweed-like dendrite inside and the outer thin shell as revealed by Figure S11a and S11c. The seaweed-like dendrites can grow tightly or loosely as revealed by Figure S11b. The loose growth pattern is more easy to reveal the inside structure but the tight growth pattern is more common according to our results.
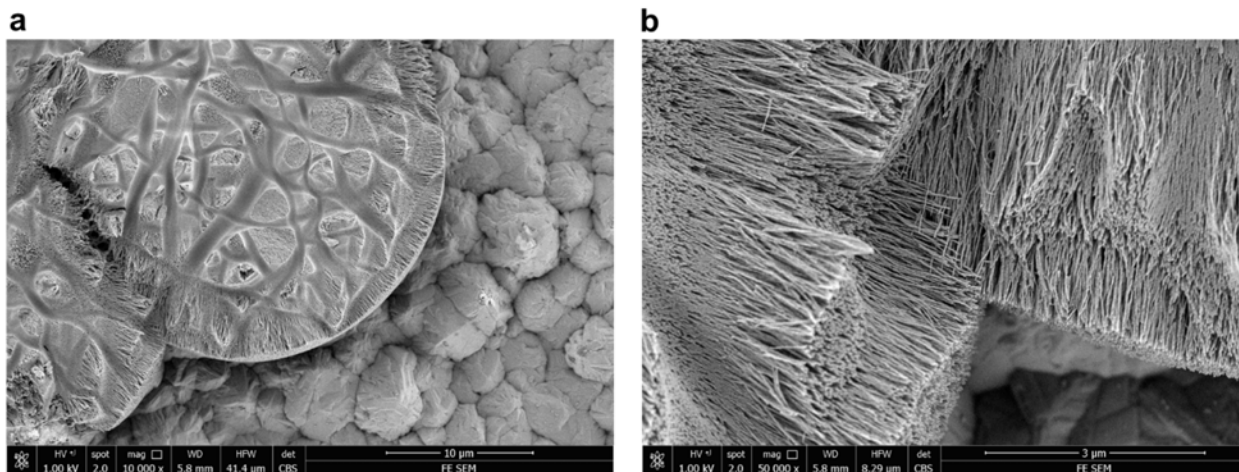
Figure S12. Microscopic morphologies of the electrodepositions from 0.4 M Mg(TFSI)$_2$/diglyme electrolyte. SEM images of the whisker-like dendritic primary nanostructures consist of extensive needle-assembling whiskers inside the spherical electrodepositions (**a**, 10000 magnifications; **b**, 50000 magnifications).

Different from the seaweed-like dendritic electrodepositions, the whisker-like dendritic electrodeposition is also observed in our next experiments with the same electrolyte systems, indicating the conflicting experimental results in this electrolyte systems. Interestingly, this whisker-like dendritic primary nanostructures also tend to grow into microspheres, which share the same sphere-on-sphere growth mode. It is also anticipated that short-circuit occurs in these cases.
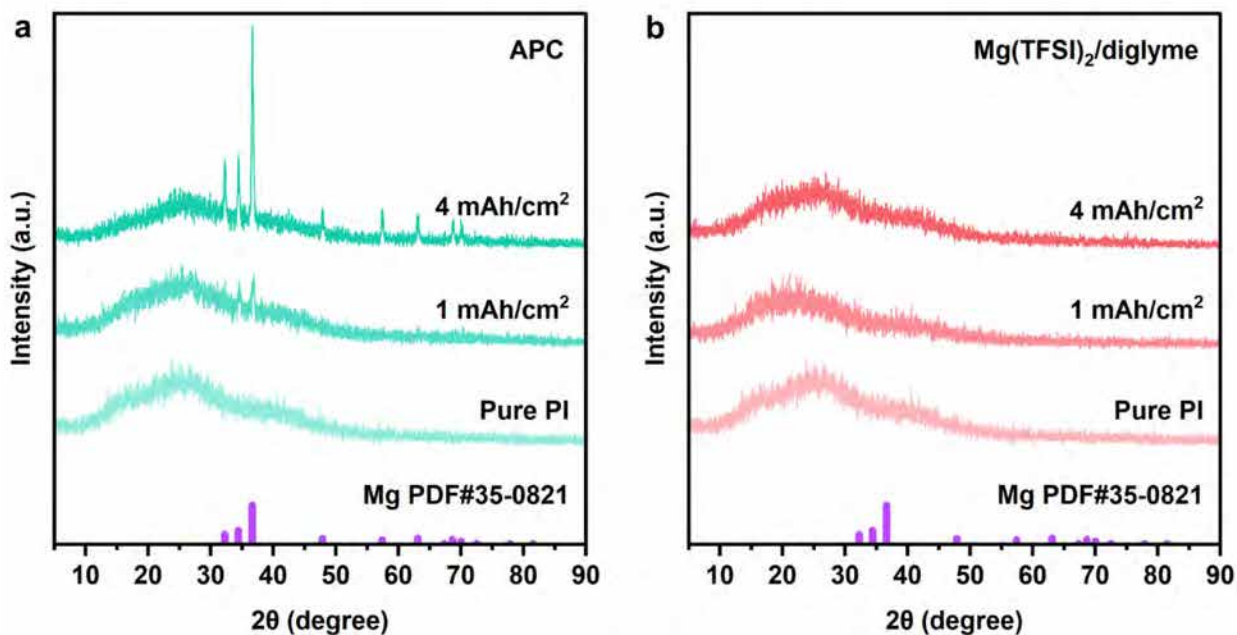
Figure S13. XRD patterns of the electrodepositions on PI separator from APC electrolyte (**a**) and Mg(TFSI)$_2$/diglyme electrolyte (**b**) with capacities of 1 mAh/cm^2 and 4 mAh/cm^2. The cell reassembling experiments (Figure S14) are conducted to accumulate electrodepositions on PI separator with capacities of 4 mAh/cm^2 from Mg(TFSI)$_2$/diglyme electrolyte for XRD characterizations.

The peaks of metallic Mg crystal signal are more noticeable with the increase of depositing capacity in the case of APC electrolytes. However, there is still no characteristic signals about metallic Mg crystals in the case of conventional Mg(TFSI)$_2$/diglyme electrolyte.
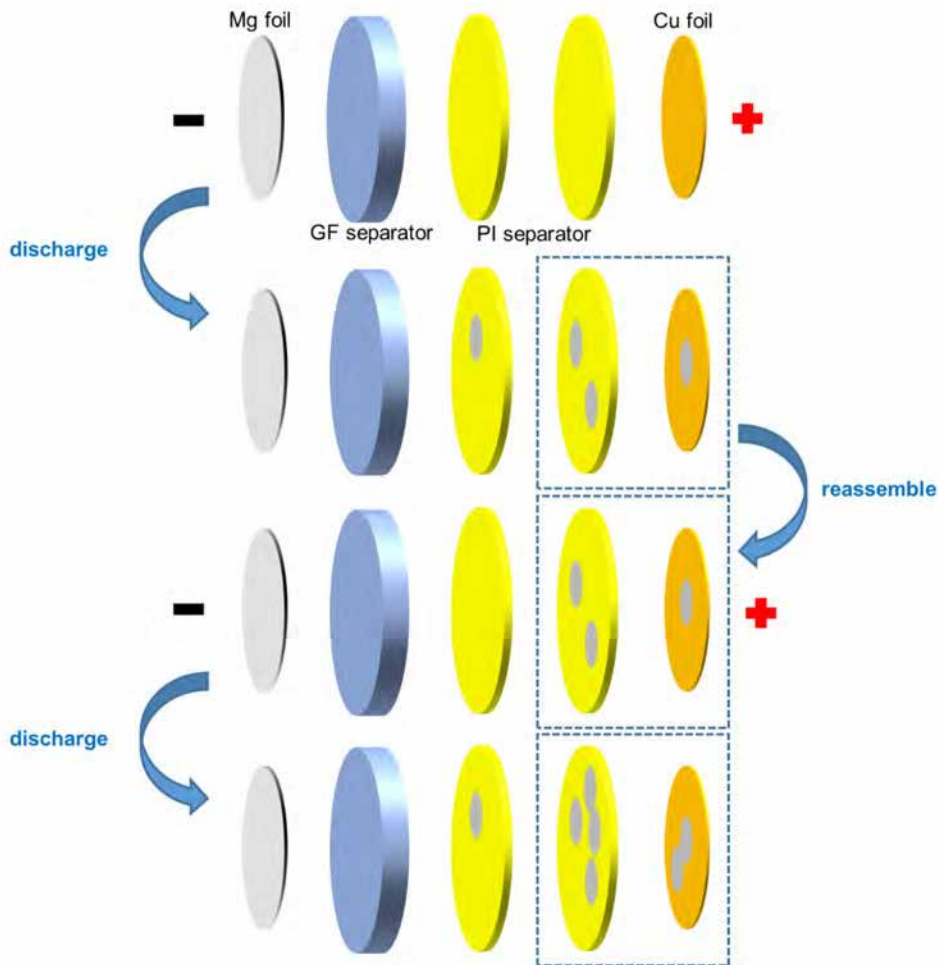
Figure S14. Schematic diagrams of the cell reassemble experiments to accumulate the electrodepositions on PI separator for XRD characterizations.

Because of the rapid short circuit of Mg//Cu cells with conventional Mg(TFSI)$_2$/diglyme electrolyte, it is difficult to generate enough electrodepositions and thus the cell reassemble experiments are conducted. Firstly, the Mg//GF(electrolytes)-PI-PI//Cu cells are assembled and discharged to generate electrodepositions on Cu foil and PI separators. Then, the Cu foil and a slice of PI separator loaded with electrodepositions are extracted and reassembled to a new cell with Mg foil, GF separator, electrolyte, and PI separator. This new cell is also discharged to continuously accumulate electrodeposition on Cu foil and PI separator. Repeating the reassemble and discharge processes to accumulate enough electrodepositions (depositing capacity of 4 mAh/cm^2) on PI separator for XRD characterization shown in Figure S13.
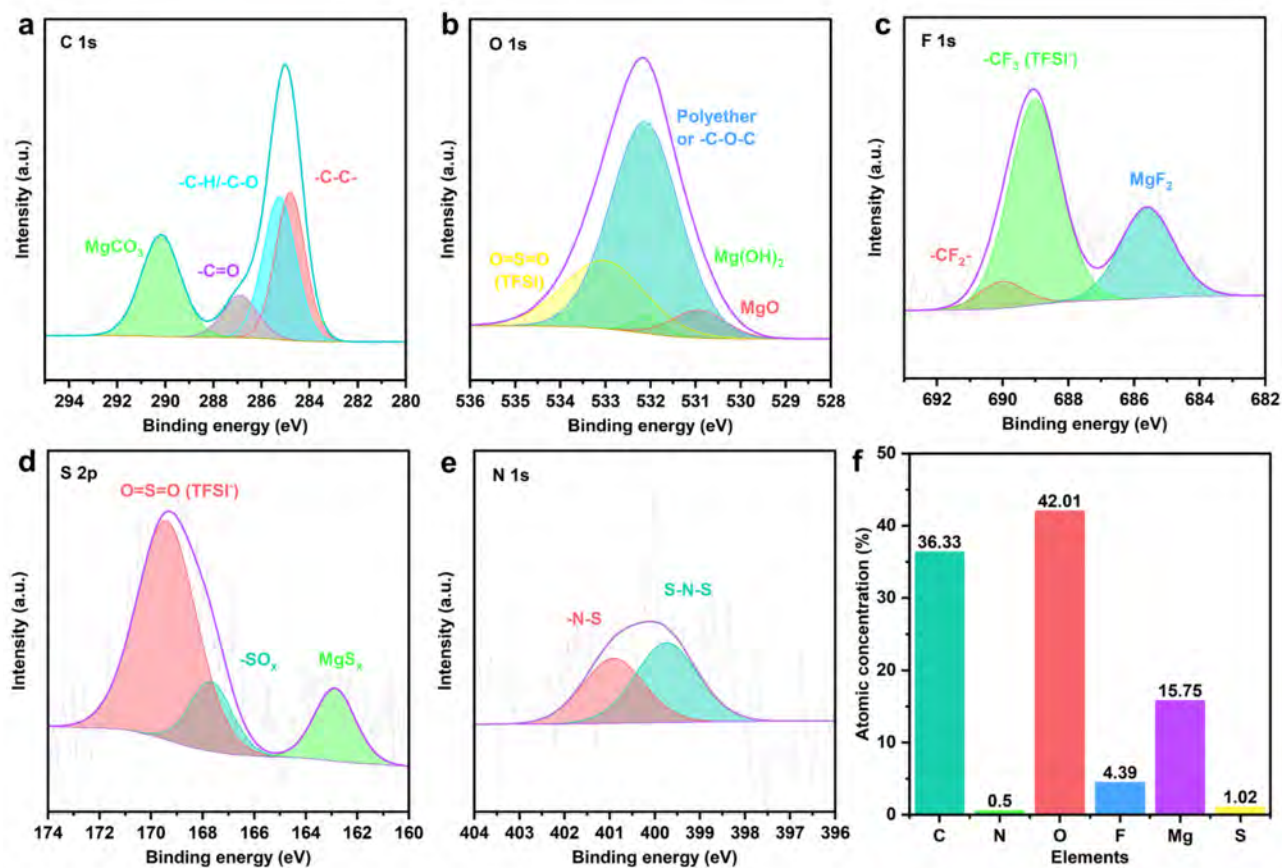
Figure S15. XPS characterizations of the electrodepositions. High resolution XPS spectra of C 1*s* (**a**), O 1*s* (**b**), F 1*s* (**c**), S 2*p* (**d**), N 1*s* (**e**), and the corresponding atomic concentration (**f**) of the electrodepositions from 0.4 M Mg(TFSI)$_2$/diglyme electrolyte.

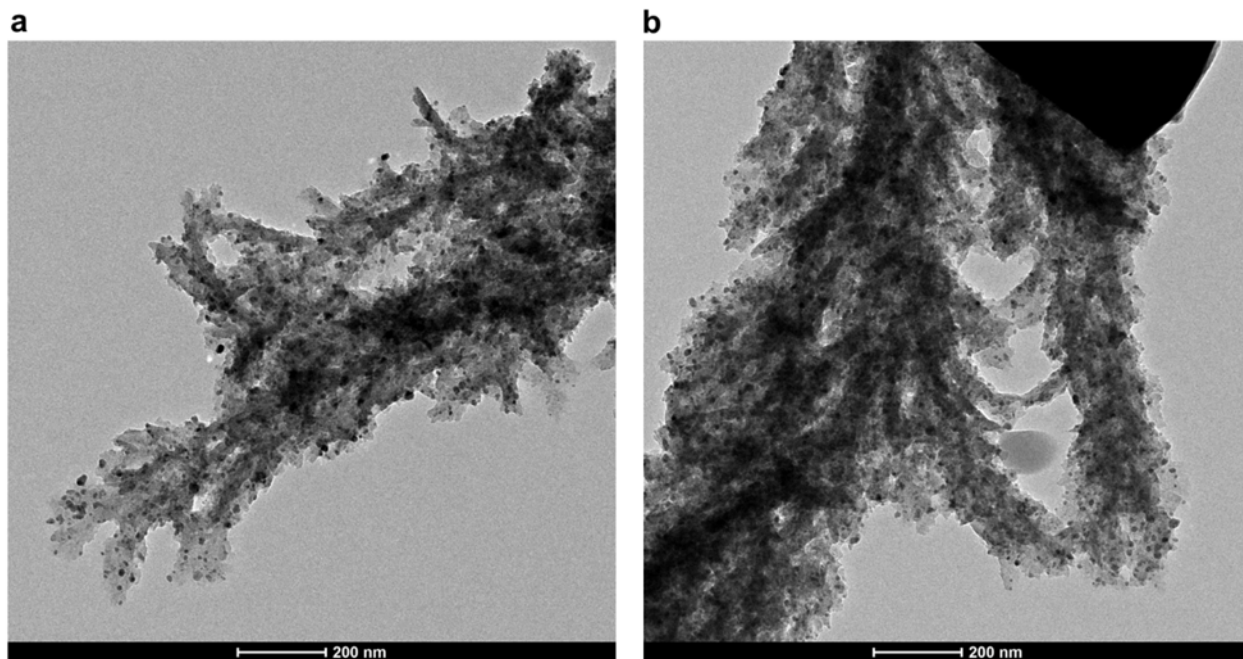**Figure S16**. Cryogenic transmission electron microscopy (Cryo-TEM) images of the electrodepositions from 0.4 M $Mg(TFSI)_2$/diglyme electrolyte.

The fractal seaweed-like dendritic electrodepositions are also detected by the Cryo-TEM images, which is consistent with the conventional SEM results (Figure 2b) and TEM results (Figure 2c).
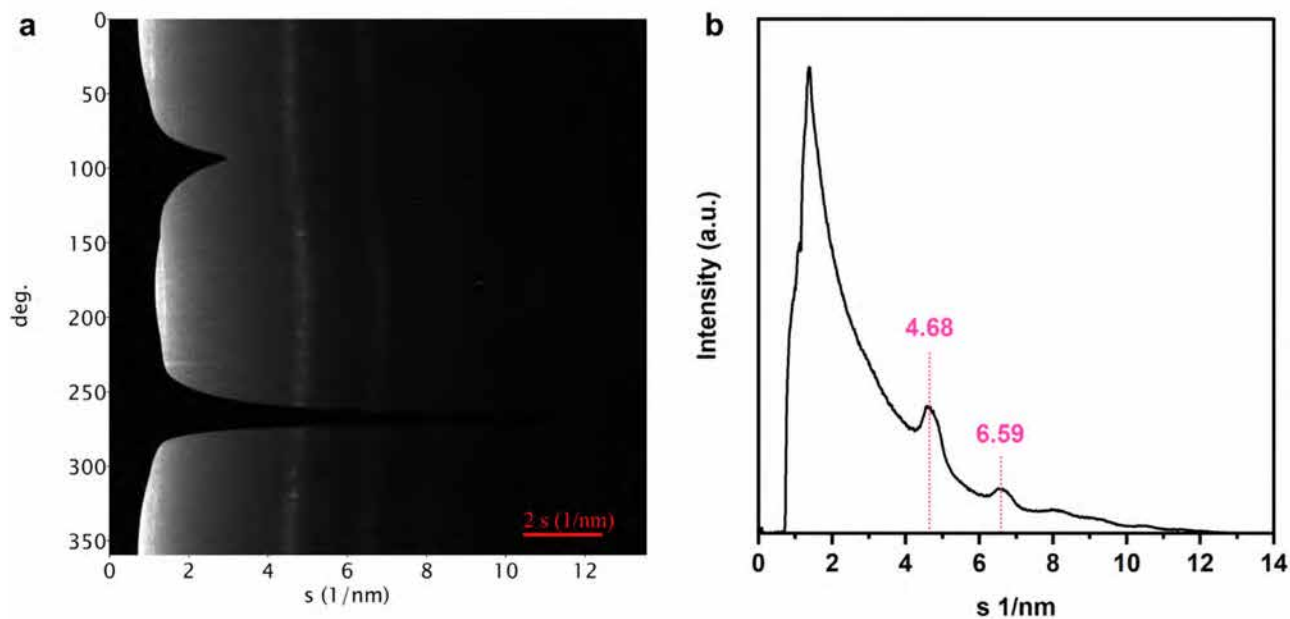
Figure S17. Linear image (**a**) and intensity profile (**b**) of SAED patterns for MgO in Figure 3h.

The diffraction center of SAED pattern is taken as the origin of polar coordinate. Transforming the expression form of SAED pattern from polar coordinates to rectangular coordinate can obtain linear image. Thus, the diffraction rings in SAED pattern are transformed to vertical lines in linear image. The intensity profile is obtained by summating the brightness of linear image. The peaks in intensity profiles reflect the diffraction rings in SAED pattern. Thus, the results of SAED become more readable and accurate. The intensity profile shows two obvious peaks of 4.68 and 6.59 nm^{-1} (i.e. 0.21 and 0.15 nm), that is, the interplanar spacing shown in SAED pattern are 0.21 and 0.15 nm respectively.
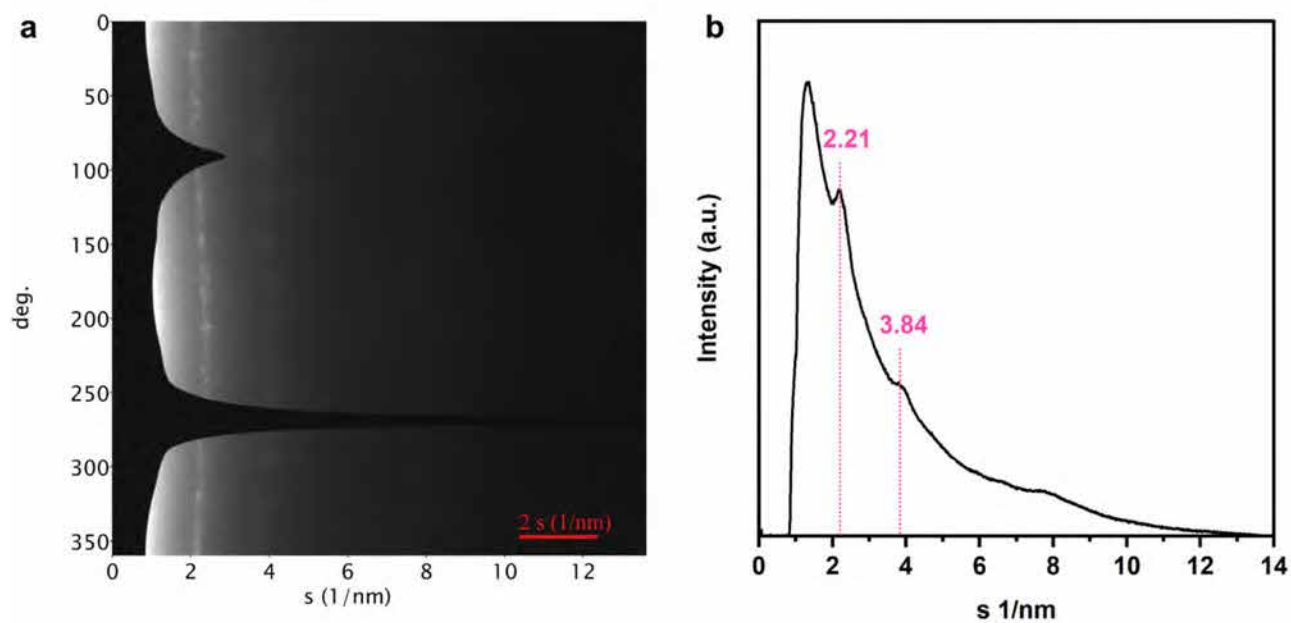
Figure S18. Linear image (**a**) and intensity profile (**b**) of SAED patterns for Mg(OH)$_2$ Figure 3i.

The intensity profile shows two obvious peaks of 2.21 and 3.84 nm^{-1} (i.e. 0.45 and 0.26 nm), that is, the interplanar spacing shown in SAED pattern are 0.45 and 0.26 nm respectively.
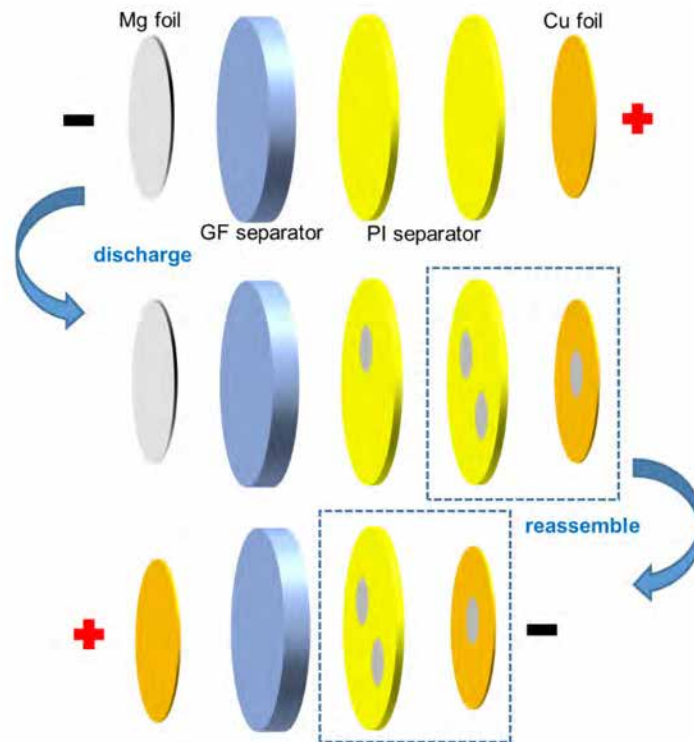
Figure S19. Schematic diagrams of the cell assembly for re-stripping experiments. Mg//GF(electrolyte)-PI-PI//Cu cells are assembled and discharged. The Cu foil and PI separator, loaded with the electrodepositions, are used as anode in the reassembled cells with alternative electrolyte.

The Mg//GF(electrolyte)-PI-PI//Cu cells are discharged to form the electrodepositions on Cu foil electrode and PI separator. The Cu foil electrode and PI separator loaded with the electrodepositions are used as anode to re-assemble cells with alternative electrolyte to evaluate their reactivity and discharge behavior.

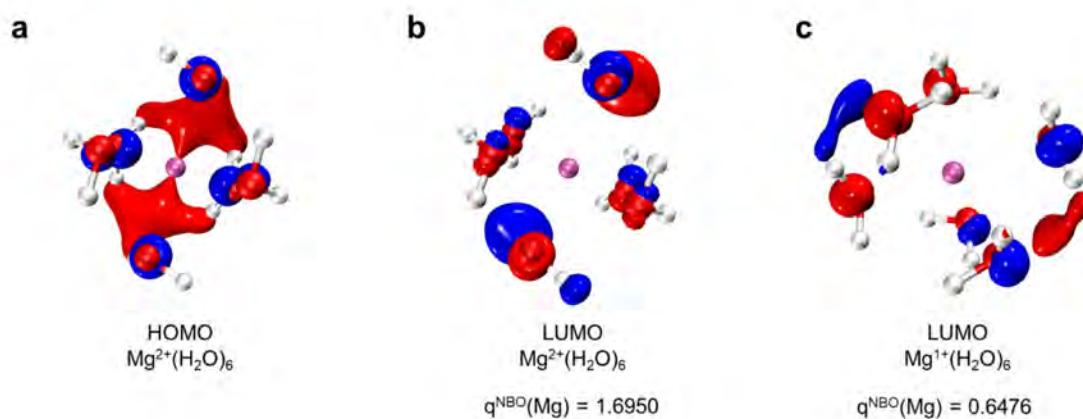**Figure S20**. Natural bond orbital (NBO) analysis of the $[Mg^{2+}(H_2O)_6]$ species in electrolyte under 1350 ppm moisture. **a-b**, HOMO (**a**) and LUMO (**b**) of the $[Mg^{2+}(H_2O)_6]$ species. The NBO value of Mg is 1.6950. **c**, LUMO of $[Mg^{1+}(H_2O)_6]$ (obtained by replacing the bivalent Mg-ion with monovalent Mg-ion). The NBO value of Mg is 0.6467.

Figure S21. NBO analysis of the $[Mg^{2+}(H_2O)_5(TFSI^-)]$ species in electrolyte under 1350 ppm moisture. **a-b**, HOMO (**a**) and LUMO (**b**) of the $[Mg^{2+}(H_2O)_5(TFSI^-)]$ species. The NBO value of Mg is 1.6169. **c**, LUMO of the $[Mg^{1+}(H_2O)_5(TFSI^-)]$ species (obtained by replacing the bivalent Mg-ion with monovalent Mg-ion). The NBO value of Mg is 0.4612.

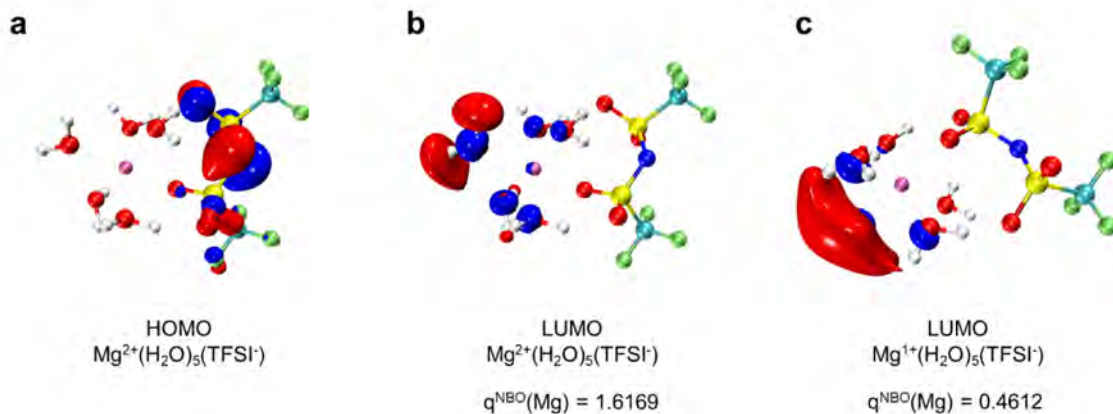|		
HOMO	LUMO	LUMO
$Mg^{2+}(diglyme)_2$	$Mg^{2+}(diglyme)_2$	$Mg^{1+}(diglyme)_2$
	$q^{NBO}(Mg) = 1.8103$	$q^{NBO}(Mg) = 0.8574$

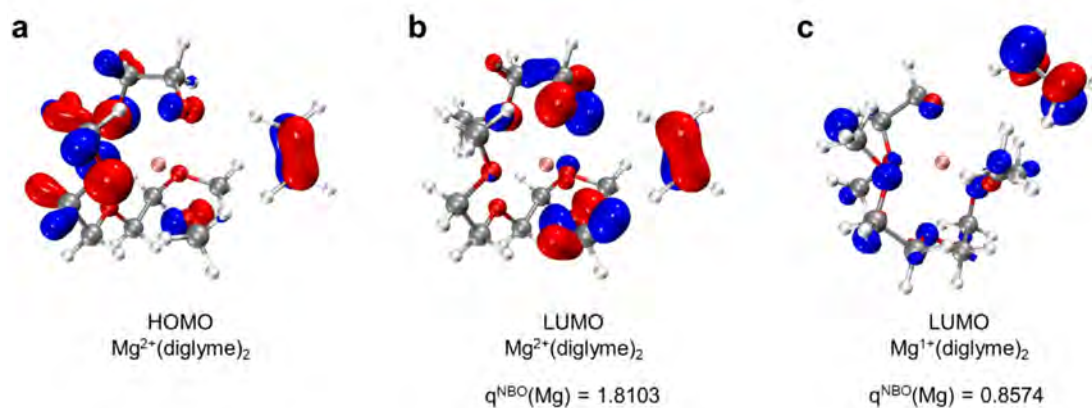**Figure S22**. NBO analysis of the $[Mg^{2+}(diglyme)_2]$ species in electrolyte under 1.35 ppm moisture. **a-b**, HOMO (**a**) and LUMO (**b**) of the $[Mg^{2+}(diglyme)_2]$ species. The NBO value of Mg is 1.8103. **c**, LUMO of the $[Mg^{1+}(diglyme)_2]$ species (obtained by replacing the bivalent Mg-ion with monovalent Mg-ion). The NBO value of Mg is 0.8574.

Figure S23. NBO analysis of the $[Mg^{2+}(diglyme)(H_2O)(TFSI^-)_2]$ species in electrolyte under 1.35 ppm moisture. **a-b**, HOMO (**a**) and LUMO (**b**) of the $[Mg^{2+}(diglyme)(H_2O)(TFSI^-)_2]$ species. The NBO value of Mg is 1.4535. **c**, LUMO of the $[Mg^{1+}(diglyme)(H_2O)(TFSI^-)_2]$ species (obtained by replacing the bivalent Mg-ion with monovalent Mg-ion). The NBO value of Mg is 0.4992.
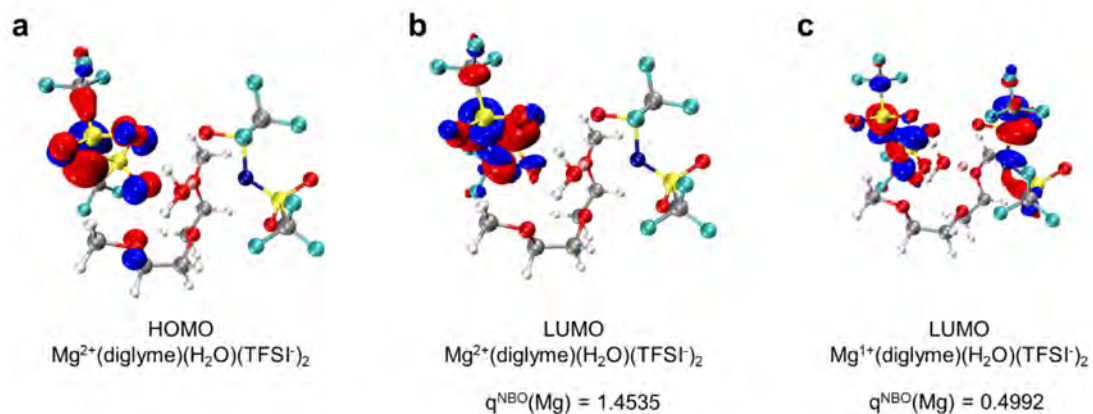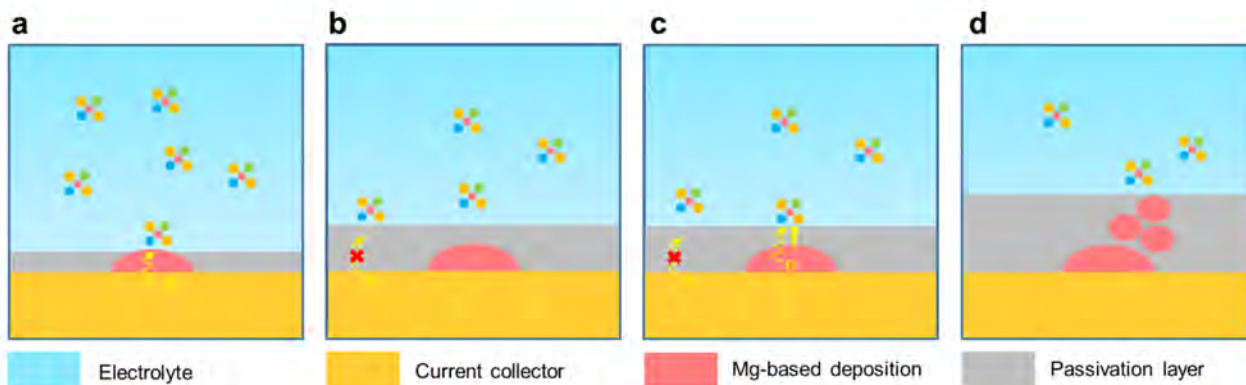
Figure S24. The evolution and formation of total mosaic-type electrodepositions.

During discharge, both active Mg^0 species and Mg^{2+}-containing inorganic components are deposited on the Cu foil electrode as shown in Figure S24a. According to our experiments of XRD and TEM results, the active Mg^0 species is easy to be buried under the passivation interphase layer (Figure S24b), which decreases the electron availability and impedes the charge transfer process. Therefore, electrons are hard to directly pass through the passivation layer to reach the current collector or the active Mg^0 crystal surface. If the passivation layer on the Mg^0 crystal protrusion is enough thin to be pierced by electrons through electron tunneling effect (Figure S24c), the new nucleation site will appear and continue to grow into total mosaic-type electrodepositions (Figure S24d) with the final sphere-on-sphere morphology.

Figure S25. Digital photos of separator after discharging. **a**, Schematic diagrams of cells used for detecting the dendrite penetration phenomenon. **b-c**, Digital photos of PI (**b**) and GF (**c**) separators after cell discharging.

The electrodepositions should be nucleated and grown on the Cu foil electrode during discharge. However, the PI separator can still be penetrated (black point region surrounded by dotted circle in Figure S25a). It is clear that the dendritic electrodepositions penetrate the PI separator and reach the Mg metal anode, leading to the cell short circuit.

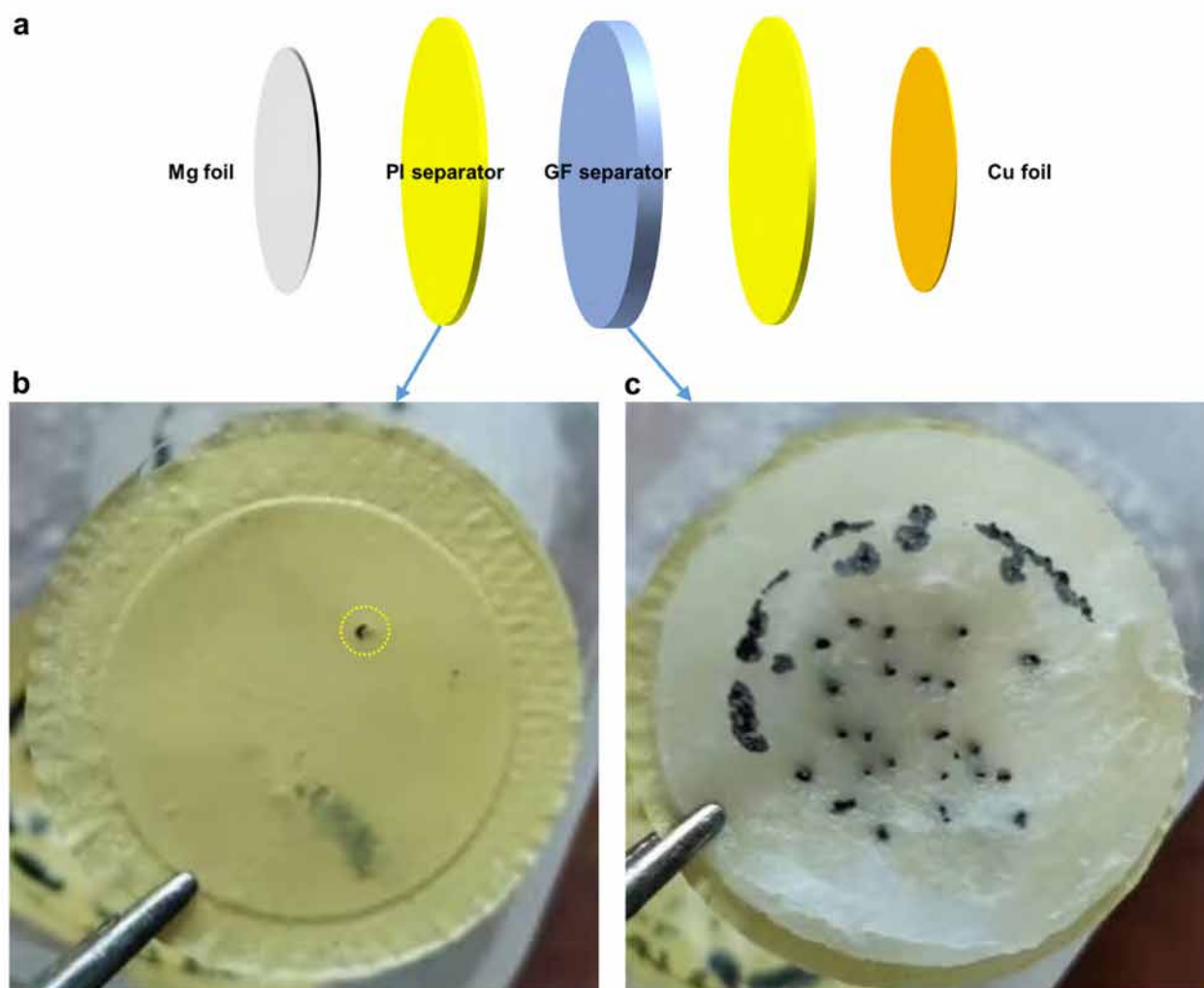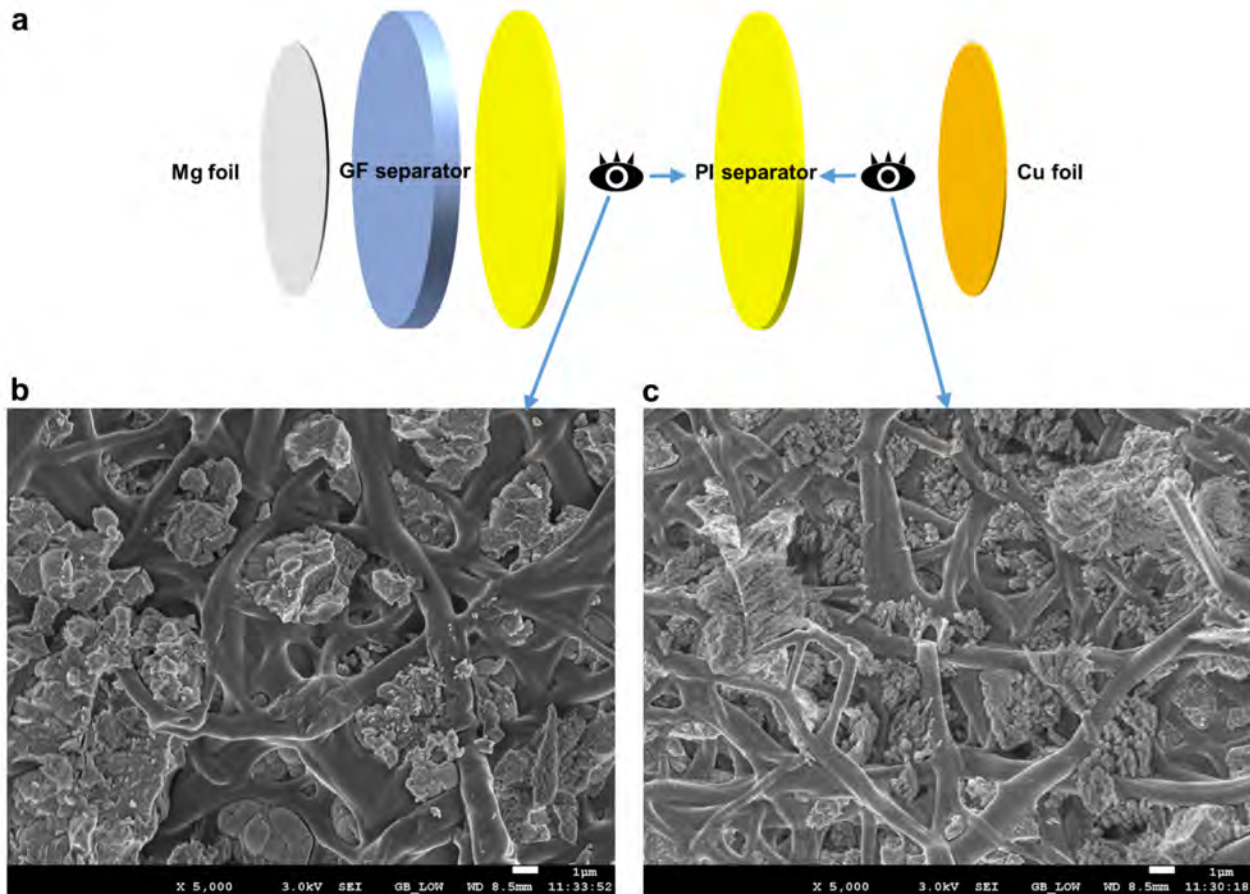**Figure S26**. Microscopic morphologies of PI separator after discharge. **a**, Schematic diagrams of cells used for detecting the dendrite penetration phenomenon. **b-c**, SEM images of both surfaces of the PI separator.

Figure S26b and c display the dendrite penetration phenomenon from microscopic scale. On both sides of the PI separator, the electrodepositions penetrate the holes of PI separator. The seaweed-like dendrite and sphere electrodepositions are all observed clearly.
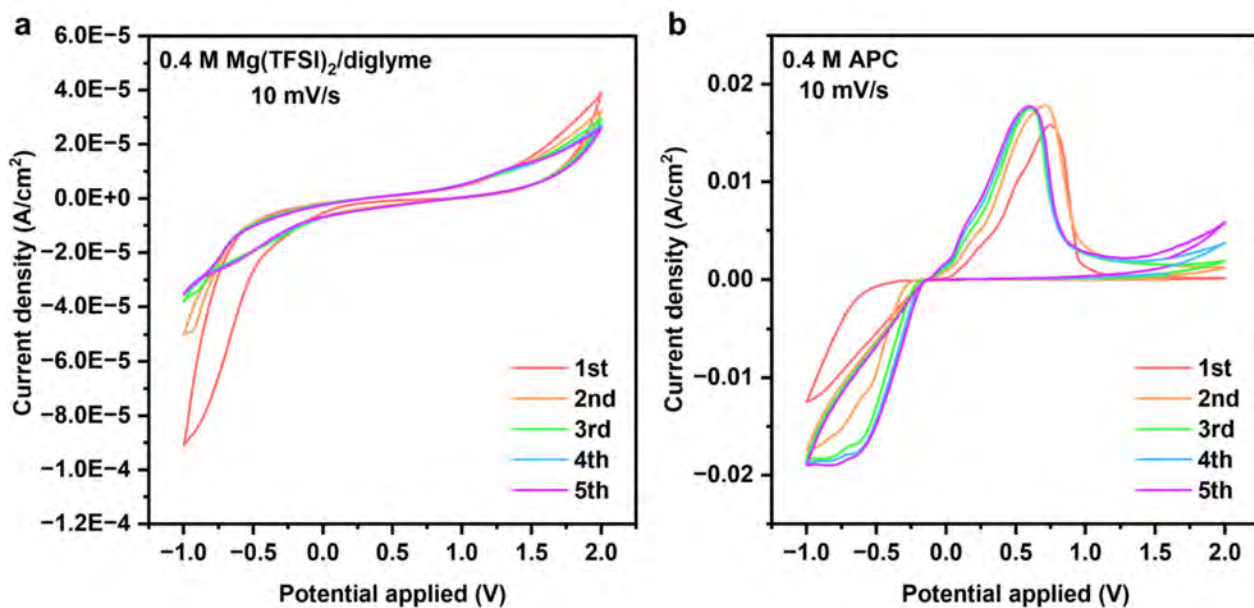
Figure S27. Cyclic voltammetry (CV) images of Mg//Cu cells with 0.4 M Mg(TFSI)$_2$-M/diglyme electrolyte (**a**) and 0.4 M APC electrolyte (**b**). Scan rate is 10 mV/s.

In the case of Mg//Cu cells with 0.4 M Mg(TFSI)$_2$-M/diglyme electrolyte, the reduction current peak intensity gradually decreases and there is no oxidation current peak. Besides, the current density of Mg(TFSI)$_2$-based battery is quite small. In contrast, the Mg//Cu cells with APC electrolyte display the Mg stripping/plating voltage peaks in Figure S27b. Thus, it can be concluded that the Mg//Cu cells with 0.4 M Mg(TFSI)$_2$-M/diglyme electrolyte cannot operate well without electrolyte modification.

Figure S28. The Mg stripping/plating performances of Mg//Cu cells based on electrolytes without/with additives. **a-f**, Voltage curves of Mg//Cu cells with varied electrolyte systems (**a**, conventional 0.4 M Mg(TFSI)$_2$/diglyme electrolyte; **b**, 0.4 M Mg(TFSI)$_2$/diglyme electrolytes with phenylmagnesium bromide additive (volume ratio of 5 to 1); **c**, 0.4 M Mg(TFSI)$_2$/diglyme electrolytes treated with Na metal; **d**, 0.4 M Mg(TFSI)$_2$/diglyme electrolytes with di-N-butylmagnesium addi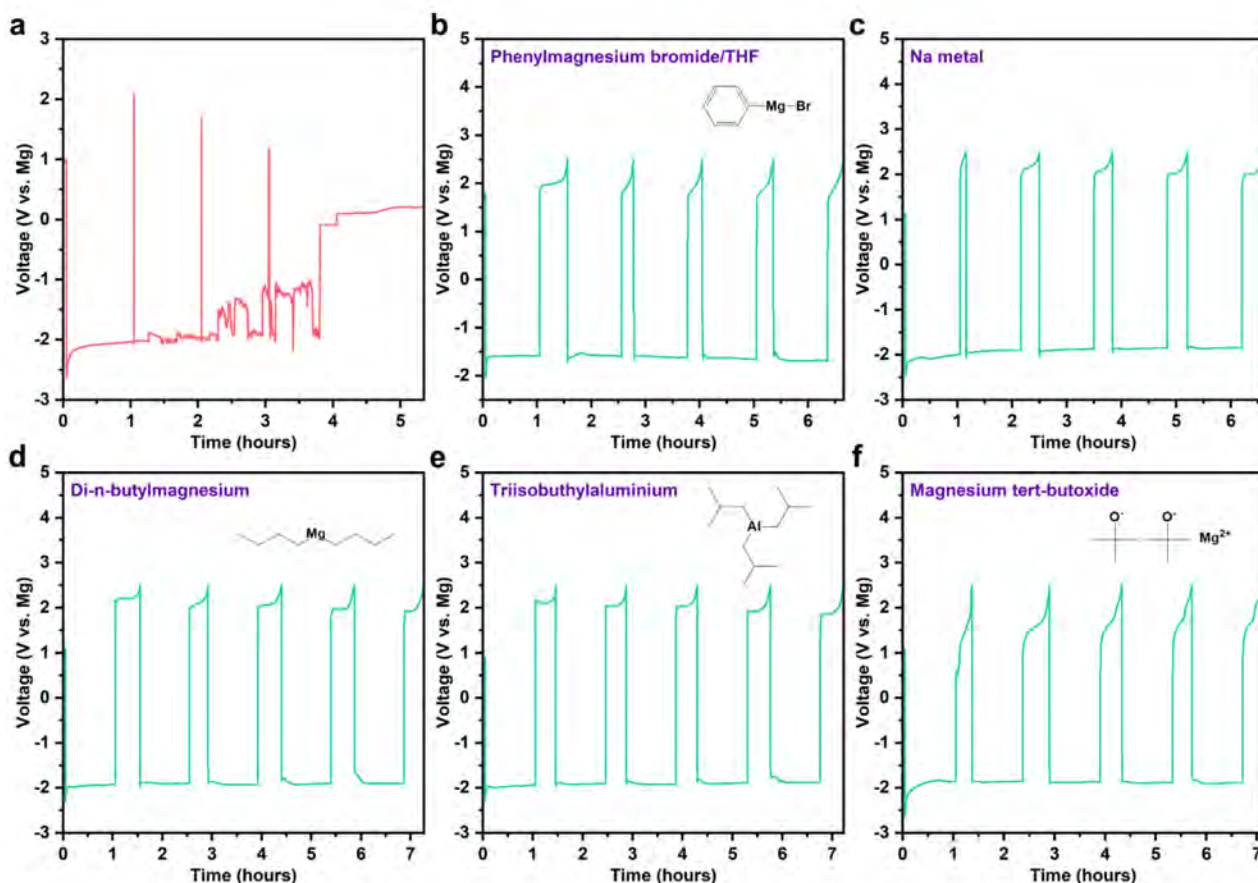tive (volume ratio of 5 to 2); **e**, 0.4 M Mg(TFSI)$_2$/diglyme electrolytes with tri-isobuthylalumminium additive; **f**, 0.4 M Mg(TFSI)$_2$/diglyme electrolytes treated with magnesium tert-butoxide (0.4 M magnesium tert-butoxide). The current density is 1 mA cm^{-2}.

To mitigate the adverse effects of trace H$_2$O impurities, varied electrolyte additives are introduced into the conventional 0.4 M Mg(TFSI)$_2$/diglyme electrolyte. By virtue of the Lewis base property and strong reducibility of Grignard reagents, the trace moisture might be reacted and consumed. Thus, several additives are selected, such as the propylmagnesium bromide, vinylmagnesium chloride, and phenylmagnesium bromide and so on. Active Mg power, Na, or K metals can also be introduced into the Mg(TFSI)$_2$/diglyme electrolyte to react with the trace moisture with the assistant of high reducibility of alkali metals. Introducing organic magnesium or aluminium reductants is another choice, such as di-n-butylmagnesium, triisobuthylaluminium, and magnesium tert-butoxide and so on. The voltage curve of Mg//Cu cells with conventional 0.4 M Mg(TFSI)$_2$/diglyme electrolyte demonstrates the poor Mg stripping/plating reversibility. The electrodepositions formed during discharge is hard to strip and the Mg//Cu cells suffer from "soft" short in 2 hours and final short circuit in 4 hours. The irreversibility might be caused by the decomposition of these H$_2$O competitively solvating ion-pairs, which results in the formation of "dead Mg"). After introducing the above

additives, the Mg stripping/plating reversibility is improved. At least, the Mg stripping/plating processes in these modified electrolytes could operate several cycles without short circuit. However, these modified electrolytes display an unsatisfied Mg stripping/plating properties, such as low Coulombic efficiencies of around 30 to 40% and high Mg plating overpotential of around 2.0 V at the current density of 1 mA cm^{-2}.
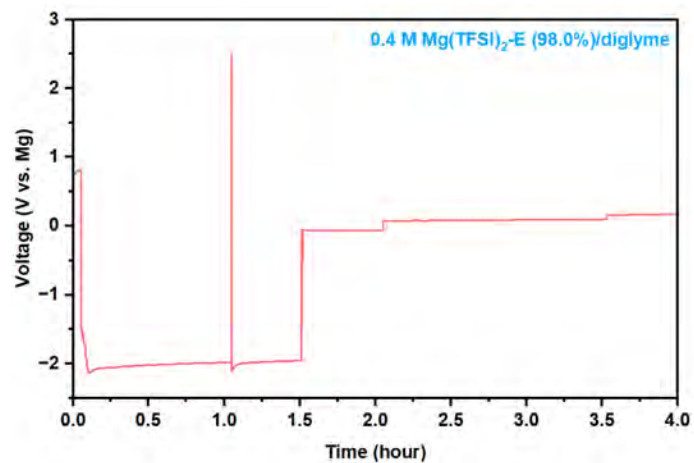
Figure S29. Voltage curve of Mg//Cu cells with 0.4 M Mg(TFSI)$_2$-E/diglyme electrolyte at the current density of 0.1 mA cm^{-2}.

The Mg//Cu cells with 0.4 M Mg(TFSI)$_2$-E/diglyme electrolyte suffers from extra-high plateau overpotential (above –2.0 V), low Coulombic efficiency (almost no charging capacity), and worse cycling performance (shorting circuit in several hours).

Figure S30. Voltage curve of Mg//Cu cells with 0.4 M Mg(TFSI)$_2$-D/diglyme electrolyte at the current density of 0.1 mA cm^{-2}.

The electrochemical performance of Mg//Cu cells with 0.4 M Mg(TFSI)$_2$-D/diglyme electrolyte is similar to the Mg//Cu cells with 0.4 M Mg(TFSI)$_2$-E/diglyme electrolyte. The differences are the slightly smaller plateau overpotential and slightly better Coulombic efficiency, which might be due to the high purity level of Mg(TFSI)$_2$-D reagent (99% for Mg(TFSI)$_2$-D vs. 98% for Mg(TFSI)$_2$-E).
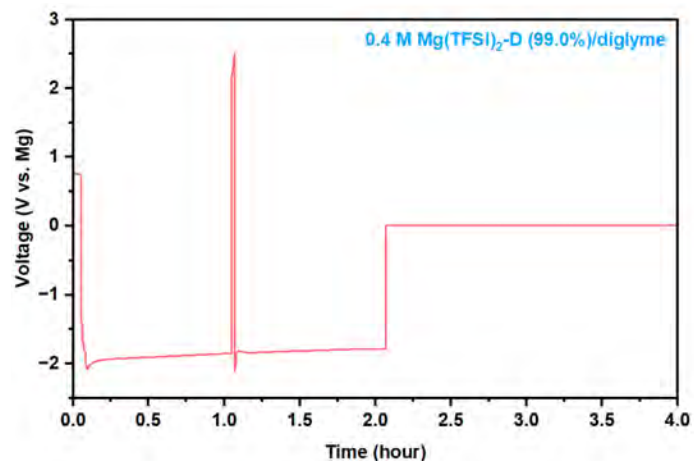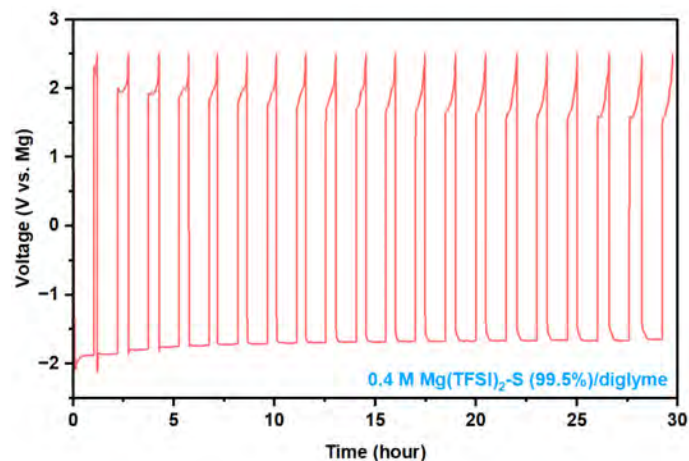
Figure S31. Voltage curve of Mg//Cu cells with 0.4 M Mg(TFSI)$_2$-S/diglyme electrolyte at the current density of 0.1 mA cm^{-2}.

Compared with Mg(TFSI)$_2$-E (98%) and Mg(TFSI)$_2$-D (99%) based electrolytes, the Mg(TFSI)$_2$-S (99.5%)/diglyme electrolyte delivers an improved Coulombic efficiency and cycling performance, and the Mg plating overpotential is also smaller. These results not only indicate the conflicting experimental results from different labs, but also suggest that the purity of the as-received salts plays a key role in achieving better Mg stripping/plating properties.
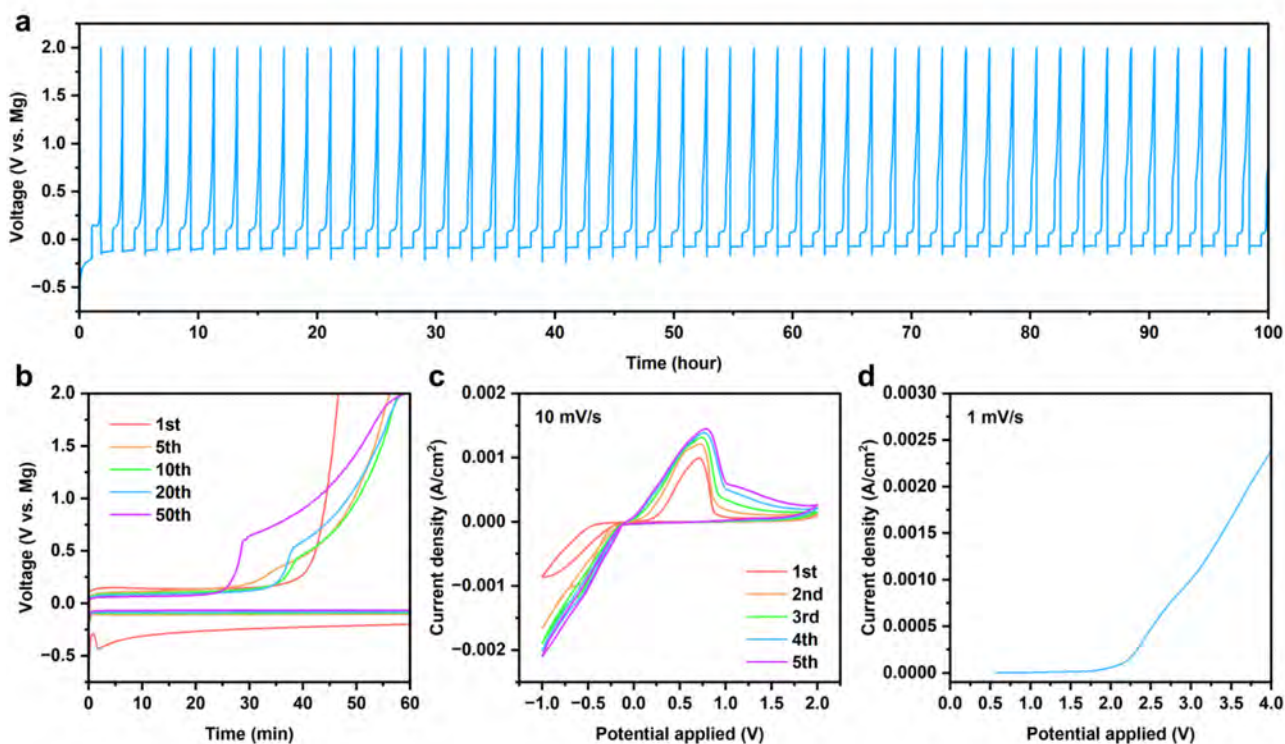
Figure S32. Electrochemical performance of Mg//Cu cells with Bu_2Mg/THF electrolyte. Voltage curves (**a** and **b**), CV (**c**), and LSV (**d**) of Mg//Cu cells with Bu_2Mg/THF electrolyte. Current density of galvanostatic charge-discharge process is 0.1 mAh/cm^{-2}.

The discharge plateau overpotential of Mg//Cu with Bu_2Mg/THF electrolyte is only about 0.1V. Nevertheless, the charging capacity of active plateau (0.1 V) decreases over cycles and the capacity contribution of another plateau (above 0.5 V) gradually increases. CV curves also indicate the proportion of second oxidation peak increases. LSV shows the anodic limit of this electrolyte is around 2.0 V. These electrochemical experiment results suggest that this Bu_2Mg/THF electrolyte is not suitable as high-voltage electrolyte systems.
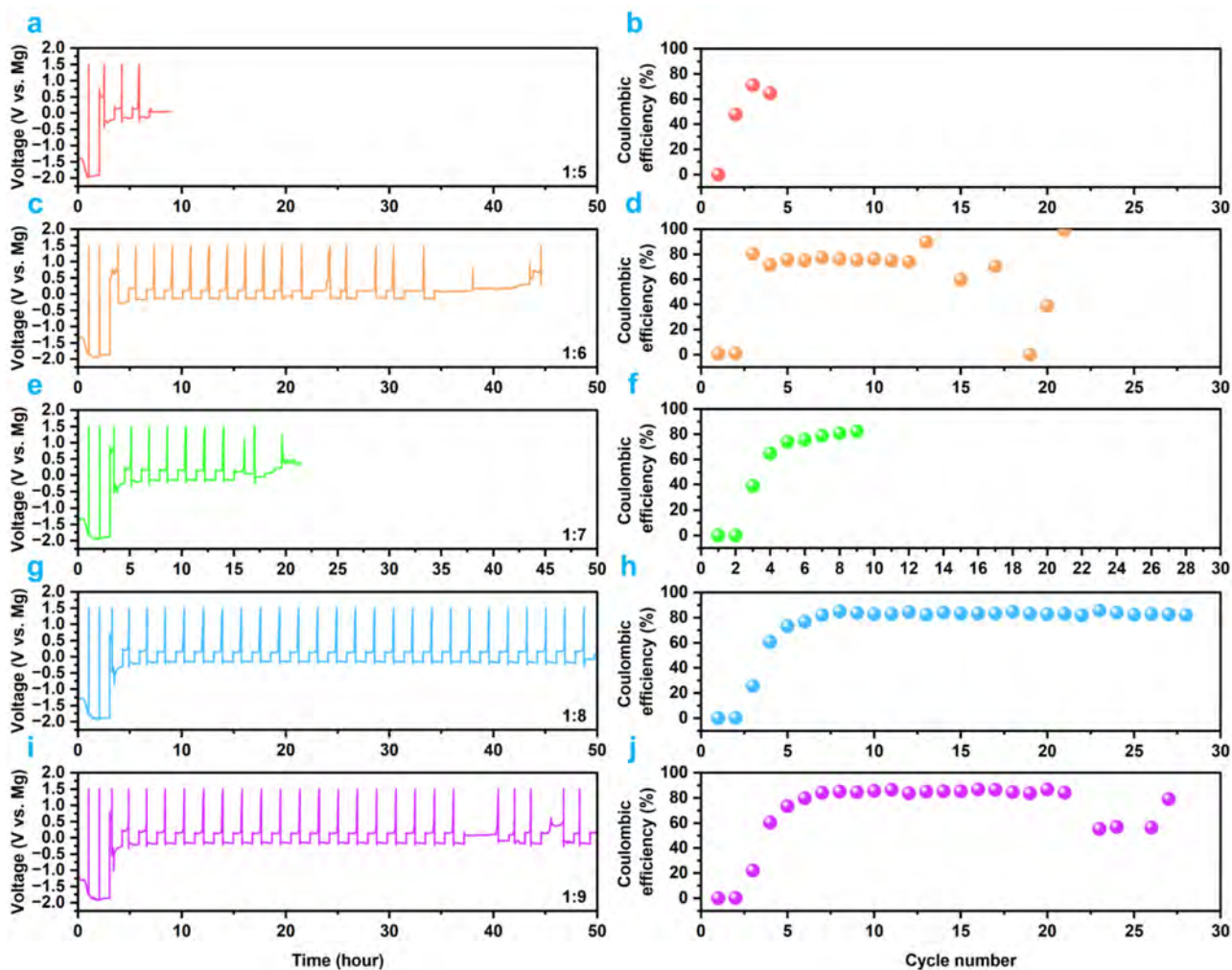
Figure S33. Mg stripping/plating performances of Mg//Cu cells with isobutylamine added Mg(TFSI)$_2$(DoDoChem)-based electrolytes. Voltage curves and corresponding Coulombic efficiency of Mg//Cu cells with Mg(TFSI)$_2$(DoDoChem)-based electrolytes with various isobutylamine additive concentrations (mol/mol$_{Mg-ion/isobutylamine}$, 1:5 (**a** and **b**), 1:6 (**c** and **d**), 1:7 (**e** and **f**), 1:8 (**g** and **h**), 1:9 (**i** and **j**)). Current density is 0.1 mAh/cm^{-2}.

With increasing the molar ratio of IBA to Mg-ions, the cycling performance and Coulombic efficiency have been improved. In the case of molar ratio of Mg-ion to IBA is 1:8, the Mg//Cu cell delivers a low plateau overpotential of about 0.15 V and an improved average Coulombic efficiency of about 83% (after 5 cycles). All of the Mg//Cu cells with only IBA additive, however, suffer from several cycles of "electrolyte conditioning process".
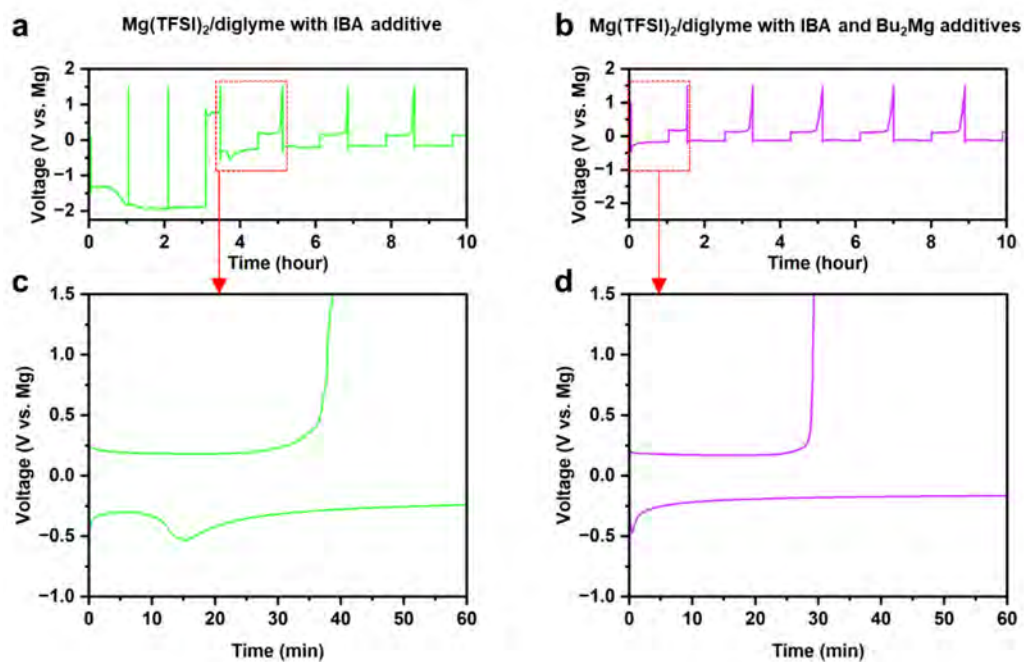
Figure S34. Effects of Bu$_2$Mg additives on the Mg stripping/plating performances of Mg//Cu cells. **a**, Voltage curve of Mg//Cu cells with Mg(TFSI)$_2$/diglyme + IBA electrolyte. **b**, Voltage curve of Mg-Cu cells with Mg(TFSI)$_2$/diglyme + IBA + Bu$_2$Mg electrolyte. **c**, Voltage curve of the 4th cycle of Mg-Cu cells with Mg(TFSI)$_2$/diglyme + IBA electrolyte. **d**, Voltage curve of the 1st cycle of Mg-Cu cells with Mg(TFSI)$_2$/biglyme + IBA + Bu$_2$Mg electrolyte. The current density is 0.1 mA cm^{-2}.

Figure S35. Prices per milliliter of electrolytes. The prices refer to Table S2. The electrolyte recipe in this work is 1 mL diglyme solvent, 0.29229 g Mg(TFSI)$_2$-D, 0.49708 mL IBA, and 25 μL Bu$_2$Mg/THF. The reference recipe is 1 mL diglyme solvent, 0.29229 g Mg(TFSI)$_2$-S and 0.22578 g 1-methoxy-2-propylamine.

Table S1. Performance comparisons of Mg//Cu cells with Mg(TFSI)$_2$-based electrolytes.

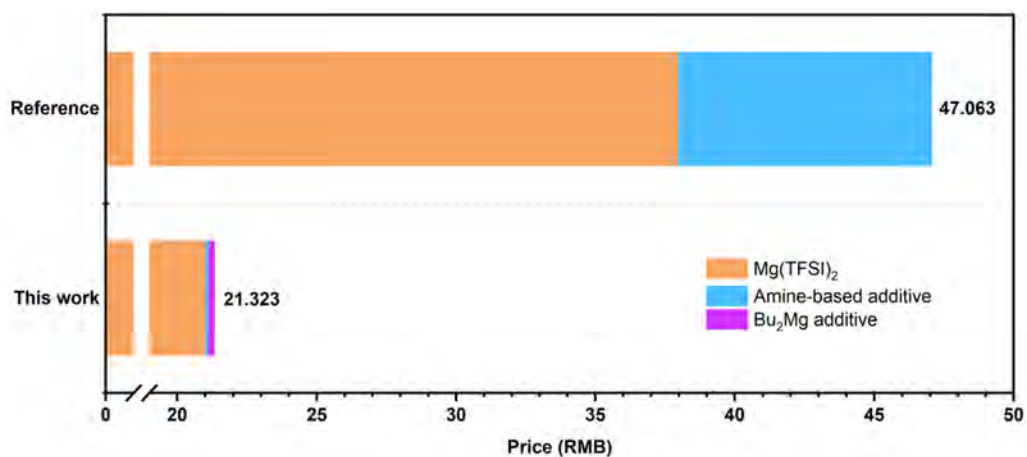| Electrolyte	Electrode	Average Coulombic efficiency (%)	Current density (mA cm^{-2})	Capacity (mAh cm^{-2})	Corresponding cycle number	Plating overpotential (V)	Ref
0.1 M Mg(TFSI)$_2$ in DME	Mg-Al	~ 10.2	0.05	0.05	30	~ –2	13
0.1 M Mg(TFSI)$_2$ and 30 mM TBABH$_4$[a] in DME	Mg-Al	17.8	0.5	0.5	23	–0.2	13
0.1 M Mg(TFSI)$_2$, 30 mM TBABH$_4$ and 20 mM MgCl$_2$ in DME	Mg-Al	21.8	0.5	0.5	29	–0.2	13
0.5 M Mg(TFSI)$_2$ and 6 mM Mg(BH$_4$)$_2$ in tetraglyme	Mg-Cu	75	1	~ 0.125	150	~ –0.25	14
0.5 M Mg(TFSI)$_2$ and 0.15 M Mg[B(OPh)$_3$H]$_2$ in diglyme	Mg-SS	74	0.044	~ 0.003.67	140	–0.23	15
0.2 M Mg(TFSI)$_2$ in DME	Mg-Cu	0.28 (1st cycle)	1	1	7	–1.38	16
0.2 M Mg(TFSI)$_2$ in DME	Mg-Cu	5.1 (1st cycle)	10	10	2	–0.54	16
0.5 M Mg(TFSI)$_2$ in DME/1-methoxy-2-propylamine (w/w 3.84/1)	Mg-SS	99.8	1.5	1.5	100	< –0.1	10
0.5 M Mg(TFSI)$_2$ in DME/1-methoxy-2-propylamine (w/w 3.84/1)	Mg-SS	99.5	0.1	0.1	100	< –0.1	10
0.4 M Mg(TFSI)$_2$ (Macklin) in diglyme	Mg-Cu	-	1	1	4	~ –2	This work
0.4 M Mg(TFSI)$_2$/diglyme and 1.0 M phenylmagnesium bromide/THF (v/v, 5/1)	Mg-Cu	27.2	1	1	24	–1.6	This work
0.4 M Mg(TFSI)$_2$/diglyme processed with Na metal	Mg-Cu	35.5	1	1	8	–2	This work

0.4 M Mg(TFSI)$_2$/diglyme and 1.0 M di-N-butylmagnesium/THF (v/v, 3/1)	Mg-Cu	38.6	1	1	13	–2	This work
0.4 M Mg(TFSI)$_2$/diglyme and 1.0 M triisobuthylaluminium/toluene (v/v, 3/1)	Mg-Cu	40.8	1	1	18	–2	This work
0.4 M Mg(TFSI)$_2$/diglyme processed with magnesium tert-butoxide	Mg-Cu	33.3	1	1	13	–2	This work
0.4 M Mg(TFSI)$_2$/diglyme and 1.0 M Bu$_2$Mg/THF (v/v, 5/1)	Mg-Cu	84	0.1	0.1	88	–0.14	This work
0.4 M Mg(TFSI)$_2$/diglyme with IBA (mol$_{TFSI}$/mol$_{IBA}$, 1/5) and 1.8 v% Bu$_2$Mg/THF	Mg-Cu	85.7	0.1	0.1	23	–0.15	This work

Table S2. The price of Mg(TFSI)$_2$ and additive reagents.

Reagent Name	Purity	Price		Brand	Ref
Mg(TFSI)$_2$	99.5%	~ 6500 RMB /50 g	130.000 RMB/g	Solvionic	This work
Mg(TFSI)$_2$	99.0%	1800 RMB /25 g	72.000 RMB/g	DoDoChem	This work
Mg(TFSI)$_2$	98.0%	1480 RMB /25 g	59.200 RMB/g	Energy Chemical	This work
Mg(TFSI)$_2$	97.0%	1696 RMB /25 g	67.840 RMB/g	Macklin	This work
Di-N-butylmagnesium 1.0 M in THF	-	665 RMB /100 mL	6.650 RMB/mL	Macklin	This work
Isobutylamine	99.5%	113 RMB /500 mL	0.226 RMB/mL	Energy Chemical	This work
1-methoxy-2-propylamine	95.0%[a]	4015.32 RMB/100 g	40.153 RMB/g	Sigma-Aldrich	10
2-methoxyethylamine	99.0%	489.11 RMB/50 mL	9.782 RMB/mL	Sigma-Aldrich	10

[a] Reagent with higher purity is more expensive. The 1-methoxy-2-propylamine used in reference is 99%.

These data were obtained at 22 August 2022.

Reference

1. S. V. Sambasivarao and O. Acevedo, *J. Chem. Theory Comput.*, 2009, **5**, 1038-1050.
2. L. Jorgensen William and J. Tirado-Rives, *Proc. Natl. Acad. Sci.*, 2005, **102**, 6665-6670.
3. L. S. Dodda, J. Z. Vilseck, J. Tirado-Rives and W. L. Jorgensen, *J. Phys. Chem. B*, 2017, **121**, 3864-3870.
4. L. S. Dodda, I. Cabeza de Vaca, J. Tirado-Rives and W. L. Jorgensen, *Nucleic Acids Res.*, 2017, **45**, W331-W336.
5. L. Martinez, R. Andrade, E. G. Birgin and J. M. Martinez, *J. Comput. Chem.*, 2009, **30**, 2157-2164.
6. H. Yang, X. Chen, N. Yao, N. Piao, Z. Wang, K. He, H.-M. Cheng and F. Li, *ACS Energy Lett.*, 2021, **6**, 1413-1421.
7. J. L. Fu, X. Ji, J. Chen, L. Chen, X. L. Fan, D. B. Mu and C. S. Wang, *Angew. Chem., Int. Ed.*, 2020, **59**, 22194-22201.
8. T. Lu, molclus program, Version 1.8.7, http://www.keinsci.com/research/molclus.html, (accessed May 2021).
9. S. Grimme, C. Bannwarth and P. Shushkov, *J. Chem. Theory Comput.*, 2017, **13**, 1989-2009.
10. S. Y. Hou, X. Ji, K. Gaskell, P. F. Wang, L. N. Wang, J. J. Xu, R. M. Sun, O. Borodin and C. S. Wang, *Science*, 2021, **374**, 172-178.
11. J. Eaves-Rathert, K. Moyer, M. Zohair and C. L. Pint, *Joule*, 2020, **4**, 1324-1336.
12. M. S. Ding, T. Diemant, R. J. Behm, S. Passerini and G. A. Giffin, *J. Electrochem. Soc.*, 2018, **165**, A1983-A1990.
13. R. Horia, D.-T. Nguyen, A. Y. S. Eng and Z. W. Seh, *Batteries Supercaps*, 2022, **5**, e202200011.
14. Z. Ma, M. Kar, C. Xiao, M. Forsyth and D. R. MacFarlane, *Electrochem. Commun.*, 2017, **78**, 29-32.
15. S. Hebié, H. P. K. Ngo, J.-C. Leprêtre, C. Iojoiu, L. Cointeaux, R. Berthelot and F. Alloin, *ACS Appl. Mater. Interfaces*, 2017, **9**, 28377-28385.
16. Z. Song, Z. Zhang, A. Du, S. Dong, G. Li and G. Cui, *J. Energy Chem.*, 2020, **48**, 299-307.